Origin of ferromagnetism and magnetic anisotropy in a family of copper(II) triangles

Logesh Mathivatanan, Guillaume Rogez, Nadia Ben Amor, Vincent Robert, Raphael G Raptis, Athanassios K Boudalis

Origin of ferromagnetism and magnetic anisotropy in a family of copper(II) triangles

Logesh Mathivatanan,[1] Guillaume Rogez,[2] Nadia Ben Amor,[3] Vincent Robert,[4] Raphael G. Raptis,[1] Athanassios K. Boudalis*[4]

[1]*Department of Chemistry and Biochemistry and the Biomolecular Sciences Institute, Florida International University, Miami, FL 33199, USA.*

[2]*Université de Strasbourg, CNRS, Institut de Physique et Chimie des Matériaux de Strasbourg (IPCMS), UMR 7504, F-67000 Strasbourg, France.*

[3]*Laboratoire de Chimie et Physique Quantiques UMR 5626, CNRS/Université Paul Sabatier - Bat. 3R1B4, 118 route de Narbonne 31062 Toulouse Cedex 09, France*

[4]*Institut de Chimie de Strasbourg (UMR 7177, CNRS-Unistra), Université de Strasbourg, 4 rue Blaise Pascal, CS 90032, F-67081 Strasbourg, France. E-mail: bountalis@unistra.fr.*

Abstract

Previously reported ferromagnetic triangles $(N^nBu_4)_2[Cu_3(\mu_3\text{-}Cl)_2(\mu\text{-}4\text{-}NO_2\text{-}pz)_3Cl_3]$ (**1**), $(PPN)_2[Cu_3(\mu_3\text{-}Cl)_2(\mu\text{-}pz)_3Cl_3]$ (**2**), $(bmim)_2[Cu_3(\mu_3\text{-}Cl)_2(\mu\text{-}pz)_3Cl_3]$ (**3**) and newly reported $(PPh_4)_2[Cu_3(\mu_3\text{-}Cl)_2(\mu\text{-}4\text{-}Ph\text{-}pz)_3Cl_3]$ (**4**) were studied by magnetic susceptometry, Electron Paramagnetic Resonance (EPR) spectroscopy and *ab initio* calculations to assess the origins of their ferromagnetism and of the magnetic anisotropy of their ground S = 3/2 state (PPN^+ = bis(triphenylphosphine)iminium, $bmim^+$ = 1-butyl-3-methylbenzimidazolium). *Ab initio* studies revealed the d_{z^2} character of the magnetic orbitals of the compressed trigonal bipyramidal copper(II) ions. Ferromagnetic interactions were attributed to weak orbital overlap *via* the pyrazolate bridges. From the wavefunctions expansions, the ratios of the magnetic couplings was determined, which was indeterminate by magnetic susceptometry. Single-crystal EPR studies of **1** were carried out to extend the spin Hamiltonian with terms which induce zero-field splitting (zfs), namely dipolar interactions, anisotropic exchange and Dzyaloshinskii-Moriya interactions (DMI). The data were treated through both a giant-spin model and through a multispin exchange-coupled model. The latter indicated that ~62% of the zfs is due to anisotropic and ~38% due to dipolar interactions. The powder EPR data of all complexes were fitted to a simplified form of the multispin model and the anisotropic and dipolar contributions to the ground state zfs were estimated.

Introduction

Triangular Molecular NanoMagnets (MNMs) comprising half-integer spins (*e.g.*, Cu^{II}, $S = 1/2$; Fe^{III}, $S = 5/2$) present particularly diverse interest. Historically, they were the first complexes for which the multispin Hamiltonian approach was properly implemented, in Kambe's seminal work.[1] Over time, their relevance has extended to various domains, ranging from biology to spintronics. E.g. their molecular and magnetic structures make them ideal models for the trimetallic active sites of various bioinorganic systems like the [3Fe-3S] centers in ferredoxins,[2,3] or the active sites of particulate Methane Monoxygenase (pMMO).[4–7] Accordingly, their reactivity has also led to their study as biomimetic catalysts.[8,9] In an entirely different context, triangular systems have been recently proposed as the basis for spintronic materials characterized by spin-chiral magnetism[10–12] and magnetoelectric couplings.[13–15]

A particularly attractive characteristic of triangular complexes is their ability to demonstrate complex magnetic phenomena, while remaining small enough for *ab initio* inspections and for exact diagonalization of the underlying spin Hamiltonian. Indeed, over the past years, advances in Molecular Magnetism have been made by considering phenomena that transcend the simple Heisenberg-Dirac-van Vleck (HDvV) picture, such as single-ion anisotropies, Dzyaloshinskii-Moriya interactions (DMI), anisotropic exchange, dipolar interactions and hyperfine interactions.[16–19] However, their consideration is usually carried out selectively for three reasons: (a) Lack of sufficiently detailed data (*e.g.* from single crystals) may pose the risk of over-parametrization. (b) Construction of a more elaborate model, including such elements as tensor orientations or non-exchange interactions (*e.g.* dipolar), is a highly non-trivial task even if the basic theory is well-understood. (c) The size of the system may pose insurmountable limitations in terms of computational cost. For the above reasons, it is often a challenging task to properly account for these individual contributions and to advance beyond the isotropic exchange scheme.

Triangular MNMs allow the full exploitation of the available experimental data without the need of resorting to approximations for their interpretation. Thus, apart from their aforementioned interest in biocatalysis and spintronics, they retain a prominent theoretical role in Molecular Magnetism, as test systems which allow us to demonstrate how we can apply elaborate models to even larger systems.

Some of us have previously reported the synthesis and properties of a series of ferromagnetic Cu^{II}_3-pyrazolate anionic triangles (Scheme 1), exhibiting quartet ($S = 3/2$) ground states characterized by a small but discernible zero-field splitting.[20–24] The origins of their ferromagnetism, and of their ground state anisotropy have been the object of theoretical studies[25] and inspections combining theory and

experiment.[26] Attempts to address the origin of magnetic anisotropy in the ground S = 3/2 states of other ferromagnetic Cu^{II}_3 complexes, have only considered anisotropic interactions[27,28] neglecting the possible effect of DMI.[29] Moreover, in these studies, the effect of dipolar interactions on magnetic anisotropy was calculated using approximate models, and considering powder or frozen solution data.

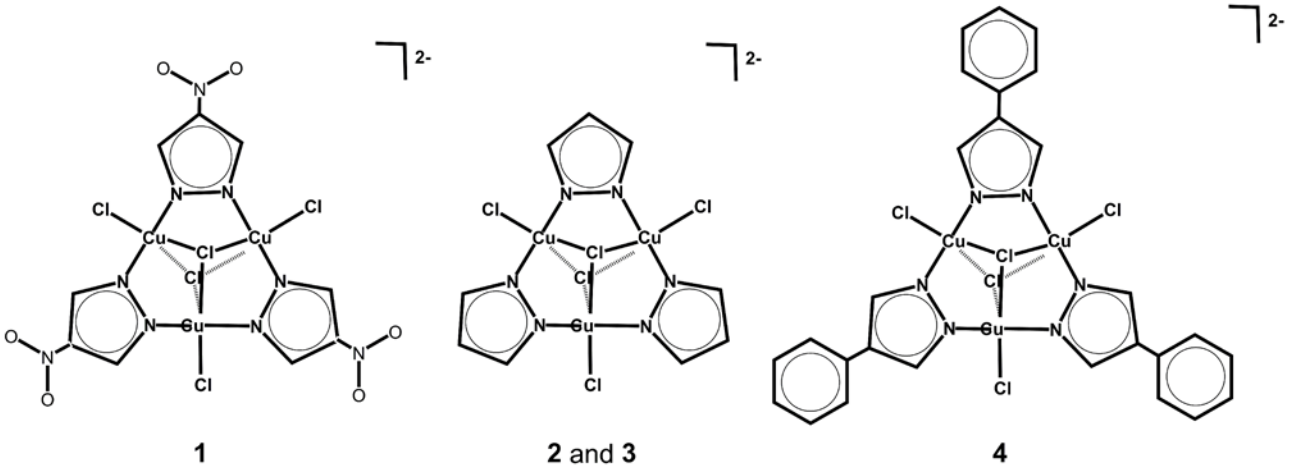

Scheme 1. The dianionic Cu^{II}_3 complexes studied in this work.

Due to the limited information derived from these previous studies on the finer terms of the spin Hamiltonians of such systems, we decided to undertake an in-depth investigation of previously reported complexes $(N^nBu_4)_2[Cu_3(\mu_3\text{-}Cl)_2(\mu\text{-}4\text{-}NO_2\text{-}pz)_3Cl_3]$ (**1**),[22] $(PPN)_2[Cu_3(\mu_3\text{-}Cl)_2(\mu\text{-}pz)_3Cl_3]$ (**2**),[20] $(bmim)_2[Cu_3(\mu_3\text{-}Cl)_2(\mu\text{-}pz)_3Cl_3]$ (**3**)[24] and the newly reported $(PPh_4)_2[Cu_3(\mu_3\text{-}Cl)_2(\mu\text{-}4\text{-}Ph\text{-}pz)_3Cl_3]$ (**4**). This investigation consists of single-crystal EPR studies of **1**, and powder and solution EPR studies of **1**-**4**. These experiments are analyzed by considering: (a) only an isolated S = 3/2 spin assigned to the ground state (the "giant spin" model) and (b) the full multispin Hamiltonian, including exchange and dipolar terms (multispin model). We also complemented those experiments with wavefunction-based *ab initio* calculations in order to rationalize the origins of the ferromagnetic ground state and to provide an analysis of the magnetic orbitals.

This work goes beyond previous studies, in that it uses single-crystal EPR data combined with exact expression of dipolar interactions to assess the relative roles of anisotropic and DM interactions in the ground-state anisotropy. Our overall strategy combines complementary techniques to extract detailed information on the spin Hamiltonian parameters, in particular, we employ: (i) Magnetic susceptometry to accurately derive average magnetic couplings. (ii) Theoretical studies to assess the ratio of the magnetic coupling constants and the character of the magnetic orbitals. (iii) EPR single-crystal studies to obtain a precise description of the magnetic anisotropy of the system's ground state. (iv) Single-

crystal structural parameters to exactly calculate the dipolar contributions to the ground-state zfs. Using this information, we are then able to assess contributions that induce zfs, in particular anisotropic exchange and DMI, while also modeling the local *g*-tensor orientations that should affect the dipolar-induced part of the zfs. This strategy provides the deepest level of detail, combining experimental and theoretical information to construct a detailed multispin Hamiltonian augmented with the exact calculation of dipolar interactions, without overparametrizing the problem.

Furthermore, considering the experimental difficulties in obtaining single-crystal EPR data on a routine basis, we test a simplified form of this model and its ability to treat powder and solution EPR spectra when single-crystal data are not available.

Results

Theoretical framework for the magnetism of spin triangles

Isotropic exchange

After Kambe's original use of an equilateral isotropic exchange (HDvV) model to interpret the magnetic properties of antiferromagnetic (AF) spin triangles,[1] an equilateral-to-isosceles symmetry breaking was considered to account for low-temperature magnetic susceptibility data.[30–32] This is known as "magnetic Jahn-Teller effect",[33] and was also considered in a dynamic context of atomic vibrations.[34,35] Moreover, low-temperature EPR data revealed the importance of DMI (antisymmetric exchange) to explain the magnetic (*g*-tensor) anisotropy of the ground state.[36–39] Numerous continuous-wave (CW) EPR studies of transition-metal spin triangles have revealed an abnormally low perpendicular *g*-tensor component ($g_\perp$), as low as 1.1.[40] This gives rise to resonances at finite magnetic fields,[3,41,42] whose values can be readily explained by assuming both an "isosceles" HDvV symmetry (*i.e.*, $J_{12} = J_{13} = J$, $J_{23} = J'$, $J \neq J'$) and a DMI-induced anisotropy. The study of ferromagnetic (FM) spin triangles, particularly through EPR spectroscopy, has benefited from the models developed for the AF ones as the theoretical context is the same,[21,23,27] although the observed behaviors are those of $S > 1/2$ states, with distinctly different experimental signatures.

Rakitin *et al.*[36] derived expressions for the energies of the magnetic multiplets associated with a scalene spin Hamiltonian of AF or FM triangles, *i.e.* one where $J_{12} \neq J_{23} \neq J_{31} \neq J_{12}$. However, an isosceles Hamiltonian is sufficient to recover and interpret experimental properties in most cases, whereas a scalene model often leads to over-parametrization. Its magnetic states are constructed from the intermediate and total spin quantum numbers S_{23} and S_T ($\hat{\mathbf{S}}_{23} = \hat{\mathbf{S}}_2 + \hat{\mathbf{S}}_3$, $S_{23} = 1$ or 0; $\hat{\mathbf{S}}_T = \hat{\mathbf{S}}_{23} + \hat{\mathbf{S}}_1$), whose energies are readily derived from the Kambe spin-coupling scheme as $E(S_{23},S_T) = (J/2)[S_T(S_T +$

1) – $S_{23}(S_{23} + 1)$] + (J'/2)$S_{23}(S_{23} + 1)$ ($\hat{H} = +J_{ij}\mathbf{S}_i\mathbf{S}_j$ formalism). For an isosceles FM triangle (J, $J' < 0$) of S_i = 1/2 ions experiencing only isotropic exchange, the magnetic structure in the $|S_T, S_{23}\rangle$ basis is characterized by a ground state quartet Q = $|3/2, 1\rangle$ (henceforth fixing its energy at $E_Q = 0$) and two excited doublet states D0 = $|1/2, 0\rangle$ and D1 = $|1/2, 1\rangle$ (with energies E_{D0} and E_{D1}, respectively). It needs to be noted that for the calculation of thermodynamic observables, such as the magnetization, any coupling scheme is valid, *i.e.* any one among $\hat{\mathbf{S}}_{12}$, $\hat{\mathbf{S}}_{13}$ or $\hat{\mathbf{S}}_{23}$ can be chosen as an intermediate spin operator, with the corresponding interaction being then described by the unique coupling constant J'. The choice of $\hat{\mathbf{S}}_{23}$ in this general example is purely arbitrary, though prior knowledge of the magnetic symmetry can make the choice less so. The corresponding energies E_{D0} and E_{D1} are functions of the exchange constants J and J' (see Table 1) and their ordering depends on the relative magnitudes of J and J': D0 ($S_{23} = 0$) is the lowest-lying doublet state for $|J| > |J'|$, and the opposite ordering holds for $|J| < |J'|$.

From the above expression it is easily shown that the spacing between the doublets D0 and D1 depends on the coupling constants difference $\Delta J = J - J'$, while their average energy depends on $J_{av} = (2J + J')/3$. An important caveat is that the determination of the coupling constants J and J' from two energies $E_1 < E_2$ for which no other information is known is not unique and one has to decide whether $|J| < |J'|$ or $|J| > |J'|$. In configuration interaction calculations (e.g. DDCI type), the wavefunction is expanded on a set of determinants (Slater determinants). In the expansions, the coefficients (or amplitudes) can be read and confronted to the ones of the model Hamilotnian to uniquely define the set of coupling constants (see below).

Table 1. Relations between doublet energies and exchange-coupling parameters J and J' ($E_Q = 0$, $+J_{ij}\mathbf{S}_i\mathbf{S}_j$ formalism[a]) for the two cases of an isosceles model, *i.e.* $|J| > |J'|$ and $|J| < |J'|$ ($\Delta J = J - J'$; $J_{av} = (2J + J')/3$). In calculating E's from J's (top), the intermediate-spin nature of the doublet states D0 and D1 is assumed known and their relative energies E_{D0} and E_{D1} are derived from the relative magnitudes of J's. In calculating J's from E's (bottom), two energy levels ($E_1 < E_2$) whose natures are not known can lead to two (J, J') pairs corresponding to the two possible isosceles systems ($|J| > |J'|$ and $|J| < |J'|$).

***E*'s from *J*'s**		
E_{D0} ($S_{23} = 0$) =	$(J + 2J')/2$	
E_{D1} ($S_{23} = 1$) =	$3J/2$	
$\Delta E_D = E_{D0} - E_{D1}$ =	ΔJ	
$E_{Dav} = (E_{D0} + E_{D1})/2$ =	$3J_{av}/2$	
***J*'s from *E*'s ($E_1 < E_2$)**	$\|J\| > \|J'\|$	$\|J\| < \|J'\|$
J =	$-2E_2/3$	$-2E_1/3$

J' =		$-(E_1 - E_2/3)$	$-(E_2 - E_1/3)$

Origin of the magnetic anisotropies of $S > 1/2$ states

Isotropic interactions cannot account for magnetic anisotropies of states with $S > 1/2$. Single-ion zfs is an often-considered refinement to the HDvV multispin Hamiltonian that accounts for such anisotropies. However, for $S = 1/2$ ions like Cu^{II} this is inapplicable since such a term cannot be defined. Therefore, interaction-induced anisotropy needs be considered.

In its most general term, the magnetic exchange is described by the Hamiltonian $\hat{H}_{ij}^{exch} = \hat{\mathbf{S}}_i^T \cdot \tilde{\mathbf{D}}_{ij}^{exch} \cdot \hat{\mathbf{S}}_j$, where $\tilde{\mathbf{D}}_{ij}^{exch}$ is a second-rank tensor which, as Erdös pointed out[43] can be decomposed into a diagonal part $\tilde{\mathbf{D}}_{ij}^{HDvV}$, multiple of the unit tensor (describing the HDvV exchange, see above), a traceless antisymmetric part $\tilde{\mathbf{D}}_{ij}^{DMI}$ (describing the DMI) and a traceless symmetric part $\tilde{\mathbf{D}}_{ij}^{ani}$ (describing the anisotropic or "pseudo-dipolar" exchange) with elements $J_{ij}^{\alpha\beta} = J_{ij}^{\beta\alpha}$ ($\alpha, \beta = x, y, z$). The "T" exponent denotes a transpose matrix, although it is often dropped for convenience. These are written in a matricial form as:

$$\hat{H}_{ij}^{HDvV} = \hat{\mathbf{S}}_i^T \cdot \tilde{\mathbf{D}}_{ij}^{HDvV} \cdot \hat{\mathbf{S}}_j = \hat{\mathbf{S}}_i^T \cdot \begin{bmatrix} J_{ij} & 0 & 0 \\ 0 & J_{ij} & 0 \\ 0 & 0 & J_{ij} \end{bmatrix} \cdot \hat{\mathbf{S}}_j = J_{ij} \hat{\mathbf{S}}_i^T \cdot \hat{\mathbf{S}}_j \quad (1)$$

$$\hat{H}_{ij}^{DMI} = \hat{\mathbf{S}}_i^T \cdot \tilde{\mathbf{D}}_{ij}^{DMI} \cdot \hat{\mathbf{S}}_j = \hat{\mathbf{S}}_i^T \cdot \begin{bmatrix} 0 & G_{ij}^z & -G_{ij}^y \\ -G_{ij}^z & 0 & G_{ij}^x \\ G_{ij}^y & -G_{ij}^x & 0 \end{bmatrix} \cdot \hat{\mathbf{S}}_j = \begin{bmatrix} G_{ij}^x \\ G_{ij}^y \\ G_{ij}^z \end{bmatrix} \cdot (\hat{\mathbf{S}}_i^T \times \hat{\mathbf{S}}_j) = \mathbf{G}_{ij} \cdot (\hat{\mathbf{S}}_i^T \times \hat{\mathbf{S}}_j) \quad (2)$$

$$\hat{H}_{ij}^{ani} = \hat{\mathbf{S}}_i^T \cdot \tilde{\mathbf{D}}_{ij}^{ani} \cdot \hat{\mathbf{S}}_j = \hat{\mathbf{S}}_i^T \cdot \begin{bmatrix} J_{ij}^{xx} & J_{ij}^{xy} & J_{ij}^{xz} \\ J_{ij}^{xy} & J_{ij}^{yy} & J_{ij}^{yz} \\ J_{ij}^{xz} & J_{ij}^{yz} & -J_{ij}^{xx} - J_{ij}^{yy} \end{bmatrix} \cdot \hat{\mathbf{S}}_j \quad (3)$$

DMI and anisotropic (or "pseudo-dipolar") interactions are exchange interactions between ions with an orbital angular momentum operator matrix element between their electronic ground and excited states. They have a common physical origin, but DMI is a first-order spin-orbit coupling (SOC) effect, anisotropic interactions are a second-order SOC effect.[27,41,44]

In addition, a non-exchange part due to magnetic dipolar interactions must be considered. In the point-dipole approximation, this is introduced through the term:

$$\hat{H}_{ij}^{dip} = \frac{\beta^2}{r_{ij}^3} \hat{\mathbf{S}}_i \tilde{\mathbf{D}}_{ij}^{dip} \hat{\mathbf{S}}_j \qquad (4)$$

where $\beta^2 = 0.433\ \mathrm{cm}^{-1}\ \text{Å}^3 = 1.2993 \cdot 10^4\ \mathrm{MHz}\ \text{Å}^3$.

The dipolar interaction tensor $\tilde{\mathbf{D}}_{ij}^{dip}$ can be decomposed into diagonal, traceless-antisymmetric and traceless-symmetric parts in a similar manner as the exchange part.[45] It is traceless and symmetric when individual *g*-tensors are parallel[46] but this symmetry is lost in the general case of non-parallel *g*-tensors.[47] The physical origins of this term are through-space interactions, which are always present irrespective of the nature of chemical bonding, even if often difficult to detect.

Due to the similarities $\tilde{\mathbf{D}}_{ij}^{dip}$ and $\tilde{\mathbf{D}}_{ij}^{ani}$ matrices (see below), it is generally a non-trivial task to deconvolute their individual contributions from spectroscopic data alone. The knowledge of the crystal structure in combination with single-crystal EPR spectra can be used to accurately model $\tilde{\mathbf{D}}_{ij}^{dip}$ and to derive *g*-tensors. $\tilde{\mathbf{D}}_{ij}^{ani}$ can then be derived by subtracting the dipolar contribution, as illustrated by Gatteschi, Bencini and Kahn in an extended series of studies on Cu^{II}_2 complexes.[48–50] These studies were facilitated by the presence of an inversion center in all but one[51] studied complexes, which simplified the calculation of $\tilde{\mathbf{D}}_{ij}^{dip}$ and, most importantly, precluded the presence of DMI. In a similar vein, it was demonstrated that the ground-state anisotropy of Fe^{III}_6 clusters could be attributed to a combination of single-ion and dipole-interaction anisotropies.[16]

The lack of an inversion center in Cu^{II}_3 triangles complicates the situation, since DMI can also be operative, sharing the same physical origin as anisotropic exchange. Solomon *et al.* used DMI to interpret the anisotropy of the ^{2}E ground state of an AF such triangle[41] and anisotropic interactions to interpret the anisotropy of the ^{4}A ground state of a FM one.[27] Similarly, Ozarowski *et al*. employed anisotropic exchange to interpret the zfs of the $S = 3/2$ ground state of a ferromagnetic Cu^{II}_3 complex, although they raised the possible role of DMI in that context.[28] It was Belinsky who analyzed in detail the mechanism through which DMI can also induce zfs in the quartet state of both antiferro- *and* ferromagnetic spin triangles.[29] In particular, in-plane components G_x, G_y of the **G** DMI pseudovector induce a zfs in the quartet state. In the presence of a mirror plane along the metallic triangle ($G_x = G_y = 0$ due to the Moriya rules), G_z can also induce zfs in the presence of a large symmetry decrease in the isotropic exchange (magnetic Jahn-Teller effect). This conclusion was used to interpret the large zfs ($D = 1.9\ \mathrm{cm}^{-1}$) in the $S = 5/2$ ground state of an antiferromagnetic $[Ru^{III}_2Mn^{II}]$ carboxylate triangle, highlighting the potentially important role of DMI in inducing zfs in $S > 1/2$ states.[52]

In the recent past, we have been interested in the synthesis and magnetic properties of spin triangles of various families, including ferro- and antiferromagnetic copper(II) pyrazolates.[20,21,24,53,54] Therefore, we felt that some additional insights should be brought onto the respective roles of DM, anisotropic and dipolar interactions in determining the zfs of ferromagnetic Cu^{II}_3 complexes.

Magnetic susceptibility studies

The magnetic susceptibility data of **1** and **2** are similar to those previously reported for **3**[24] and $(Bu_4N)_2[Cu_3(\mu_3\text{-}Cl)_2(pz)_3Cl_3]$, characterized by 300 K values (**1**: 1.35 $cm^3\ mol^{-1}\ K$; **2**: 1.44 $cm^3\ mol^{-1}\ K$) slightly above that of three non-interacting $S = 1/2$ ions (1.24 $cm^3\ mol^{-1}\ K$ for $g = 2.1$), which increase upon cooling down to 10 K to a maximum value typical of a $S = 3/2$ system (2.1-2.2 $cm^3\ mol^{-1}\ K$), before dropping slightly upon further cooling. Magnetization isotherms collected at 1.8 K show the onset of saturation above 5 T near 3.0 $N_A\mu_B$.

These observations are consistent with ferromagnetic interactions stabilizing an $S = 3/2$ ground state with $g > 2$. Simultaneous fits to the magnetic susceptibility and isothermal magnetization data were carried out considering purely isotropic interactions (equilateral and isosceles models). These fits were of very high quality, with the isosceles models converging to equilateral ones during minimization, indicating that the error function is not sensitive to the difference $\Delta J = J - J'$, but only on the average J_{av} value.

These preliminary fits could not account for the low-T decrease of the $\chi_M T$ product, which is usually attributed to the combined effect of zfs in the ground state, intermolecular interactions and saturation of the magnetization due to Zeeman interactions. Full matrix diagonalizations allowed to explicitly account for the saturation effects, but failed to reproduce this low-T drop. This indicated that the zfs in the ground state and/or intermolecular interactions needed to be considered. The introduction of a ground state zfs through DMI or anisotropic interactions only marginally improved the agreement to the low-T data, even for unrealistically large interactions. Inclusion of DMI modulates the energies of the excited doublets and induces anisotropy in those states, which decrease their $g_\perp$ and drastically decrease their susceptibilities on the magnetic xy plane. However, magnetic susceptibility measurements on powder samples, such as ours, are less revealing of such effects. Moreover, since the net magnetization depends on the Boltzmann populations of a multitude of states, these effects are masked by the magnetization of the quartet state which is not affected by DMI (also see EPR Spectroscopy). Indeed, simulations revealed marginal effects of DMI on the calculated curves of ferromagnetic triangles.

On the other hand, consideration of weak intermolecular interactions through a mean-field correction yielded excellent agreement with the low-T data. The simplified spin-Hamiltonian that successfully fitted the magnetic susceptibility data was $\hat{H} = J\sum_{i,j=1}^{3}\hat{\mathbf{S}}_i \cdot \hat{\mathbf{S}}_j + zJ\langle S_z\rangle\hat{S}_z + \mu_B\mathbf{H}\sum_{i=1}^{3}\tilde{\mathbf{g}}_i\hat{\mathbf{S}}_i$ (5). The experimental data and fits are shown in Figure 1 and the best-fit parameters according to that model are shown in Table 2.

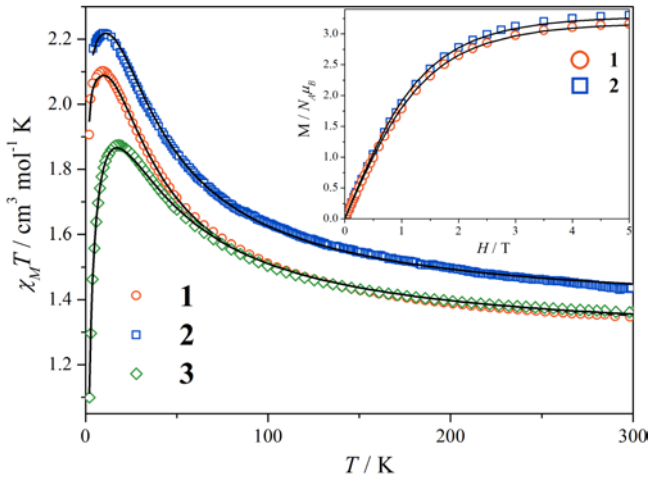

Figure 1. Experimental $\chi_M T$ *vs.* T plots for complexes **1**-**3** and best-fit curves according to the model described in the text. The inset shows the M *vs.* H experimental data and best-fit curves for complexes **1** and **2**.

Table 2. Best-fit parameters of the magnetic susceptibility data according to the model described in the text (J < 0 corresponds to a ferromagnetic interaction), given with ±5% confidence intervals calculated by *Phi*.

Complex	Ref	J	g	zJ
1	This work	−26.9(1)	2.125(1)	0.0252(8)
2	This work	−28.74(8)	2.195(1)	0.0382(1)
3	[24]	−31.23(9)	2.124(1)	0.414(1)
$(Bu_4N)_2[Cu_3(\mu_3\text{-}Cl)_2(pz)_3Cl_3]$	[23]	−28.6		

Our choice to model the $\chi_M T$ drop by intermolecular interactions instead of zfs, is validated by the observation that the intensity of this drop for each complex does not reflect the magnitudes of their zfs D parameters as determined by EPR spectroscopy (see below). This indicates that zfs effects of this

scale are not discernible by magnetic susceptometry, but require the use of more sensitive techniques, such as EPR spectroscopy.

Theoretical calculations

Conducting wavefunction-based calculations provides insights into the low-energy ordering, the nature of the spin states and the exchange coupling constants governing an isotropic HDvV Hamiltonian. Moreover, it is particularly insightful to compare the geometrical picture based on the Cu-Cu distances with the magnetic pattern that emerges from the expansion of the wavefunctions using localized MOs. To obtain such an understanding, we carried out calculations at the best level (*i.e.* DDCI3, see Supporting Information) in the philosophy of the Difference Dedicated Configuration Interaction method. The calculations were based on the published structures of complexes **1** (CCDC 208594)[20] and **2** (CCDC 628908).[22] The asymmetric unit of **2** contains two complex molecules, hereafter noted **2a** (containing atoms Cu1/2/3) and **2b** (containing atoms Cu4/5/6), and which were analyzed separately. The calculated energy values of the different magnetic states are summarized in Table 3.

The first notable finding was that for all three systems (**1**, **2a**, **2b**), the excited doublet states D0 and D1 are not degenerate, suggesting that the HDvV Hamiltonian should contain at least two coupling constants. This conclusion agrees with previous ac susceptibility[23] which had revealed a slow magnetic relaxation analysed by an Orbach relaxation through *two* excited states. This analysis indicated $\Delta J = 6.7$ cm^{-1}, which is very close to our calculations (see Table 3). Broken-symmetry DFT (BS-DFT) analysis of that complex could not predict such an energy splitting, calculating a unique J value. Moreover, this value (-139.2 cm^{-1} in the $+J_{ij}\hat{\mathbf{S}}_i\hat{\mathbf{S}}_j$[25]) varies significantly from the experimentally determined one (-28.6 cm^{-1} in the $+J_{ij}\hat{\mathbf{S}}_i\hat{\mathbf{S}}_j$ formalism[21]), prompting us to remain confident in the validity of our findings.

At this level of analysis we have not yet determined the ordering of the two doublets, each of which is characterized by a different intermediate spin value, and whose knowledge can be used to reveal the magnetic symmetry of the complex at hand (*i.e.* whether $|J| > |J'|$ or $|J| < |J'|$). Such determinations cannot be made *a priori*, but they are possible by analyzing the *ab initio* expansions in terms of Slater determinants (i.e. configurations) of the doublet states D0 and D1. The amplitudes of the determinants entering in the wavefunctions are given in the Supporting Information. In carrying out this analysis, we restrict ourselves to an isosceles (C_2) magnetic symmetry and we calculate the J and J' parameters according to the relations in Table 1 ($+J\hat{\mathbf{S}}_i\hat{\mathbf{S}}_j$ formalism), for both isosceles models ($|J| > |J'|$ and $|J| < |J'|$). This approach permits comparisons and avoids over-parametrization.

Carrying out such analysis for complex **1**, reveals that the calculated magnetic couplings do not directly reflect the structural parameters, if one only considers intermetallic distances (r_{ij}). As shown in Figure 2, whereas the intermetallic distances can be idealized in an *obtuse* isosceles triangle with the C_2 axis passing through the Cu1 atom, the wavefunction analysis indicates a $|J| < |J'|$ magnetic isosceles symmetry, with the magnetic C_2 axis passing through the Cu3 atom, meaning that $J' = J_{12}$. Assigning shorter triangle sides to stronger interactions, which implies accepting a direct causal link between r_{ij} and J_{ij}, leads to an *acute* isosceles triangle. However, direct magnetostructural correlations based on intermetallic distances are too simplistic to predict the strengths of the magnetic couplings. Similarly for **2a**, although the structural and magnetic C_2 axes coincide, the isosceles symmetries are acute and obtuse, respectively. In **2b**, the analysis of the wavefunctions of D0 and D1 indicates a strong deviation from a magnetically isosceles system, but for ease of comparison with **1** and **2a**, we present an isosceles approximation closest to the magnetic symmetry of **2a**.

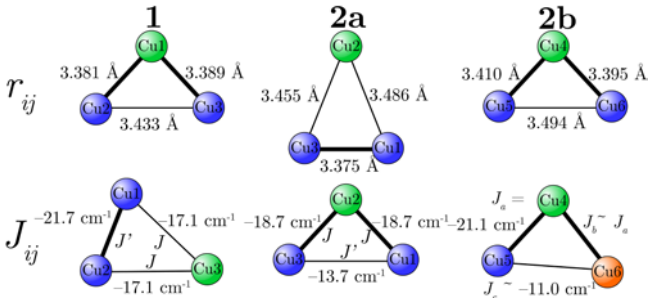

Figure 2. Indicative comparison of the structural symmetries of **1**, **2a** and **2b** (based on intermetallic distances) with their magnetic symmetries as determined from analysis of the wavefunctions of D0 and D1. Thick lines indicate shorter intermetallic distances (top row) or stronger magnetic couplings (bottom row), and the green atom indicates the apex of the isosceles triangle in each case. The discrepancies between the structural and magnetic symmetries indicate the unsuitability of simple structural considerations to predict magnetic coupling strengths. Atom numberings are those of the published structures.

Table 3. Energies in cm^{-1} of the doublet states with respect to the quartet state Q (E_Q = 0) for **1**, **2a** and **2b**. Exchange coupling constants J_{calc} and J'_{calc} are extracted for the two types of isosceles magnetic symmetries. For either symmetry, $J_{av(calc)}$ and ΔJ_{calc} are identical. In bold, the attribution based on the *ab initio* expansions of the doublet states D0 and D1 wavefunctions as linear combination of Slater determinants wavefunctions. Although indeterminate by magnetometry studies, "experimental" ΔJ values can be estimated from ΔJ_{calc} based on the $J_{av(exp)}/J_{av(calc)}$ ratio.

Complex	**1**	**2a**	**2b**[a]
E_1	25.6	23.1	21.5
E_2	30.2	28.1	31.6
J_{calc} / J'_{calc}	−20.1 / −15.5	**−18.7 / −13.7**	**−21.1 / −11.0**
	−17.1 / −21.7	−15.4 / −20.4	−14.3 / −24.4
$J_{av(calc)}$	−18.60	−17.1	−17.7
ΔJ_{calc}	+4.60	−5.0	±10.1
$J_{av(exp)}$	−27.0	−28.8	−28.8
$\Delta J_{"exp"}$[b]	**+6.68**	**−8.42**	**−16.4**

[a]Attribution of magnetic symmetry closest to that of **2a**. [b]$\Delta J_{"exp"} = \Delta J_{calc} \times (J_{av(exp)}/J_{av(calc)})$

Another important conclusion, which is directly related to the rationalization of magnetic exchange strengths and to the symmetry of the molecular *g*-tensor (see below), concerns the magnetic orbitals of the copper(II) ions. Qualitatively, such an analysis can be carried out using Addison's criterion:[55] if α and β are the two largest L-M-L angles, the trigonality index $\tau_5 = (\alpha-\beta)/60$ indicates an ideal square pyramid for $\tau_5 = 0$, and an ideal trigonal bipyramid for $\tau_5 = 1$. E.g., in the case of **1** this criterion would suggest that atoms Cu1 and Cu2 are closer to square pyramidal ($\tau_5 = 0.22$), whereas Cu3 is halfway between square pyramid and tbp ($\tau_5 = 0.57$). On the other hand, inspection of the bond lengths would also indicate that all three atoms are characterized by significantly compressed bonds along the N-Cu-N axes, and markedly elongated C-Cl bonds in the equatorial plane. This would suggest that all three coordination polyhedra are better described as compressed tbp, which are known to endow Cu^{II} ions with a $(d_{z^2})^1$ ground state, making d_{z^2} their magnetic orbitals, instead of the $d_{x^2-y^2}$ ones in square pyramidal environments.

The ambiguity of this qualitative assessment is readily resolved by our calculations which confirm that the magnetic orbitals are mostly of d_{z^2} character localized on copper(II) ions (Figure 3). One consequence of this is that the superexchange pathways primarily pass through the pyrazole ligands and

not through the μ_3-chlorides. The resulting poorly effective superexchange pathways can very well rationalize the ferromagnetic interactions since they do not allow the development of the antiferromagnetic part of the exchange interaction.

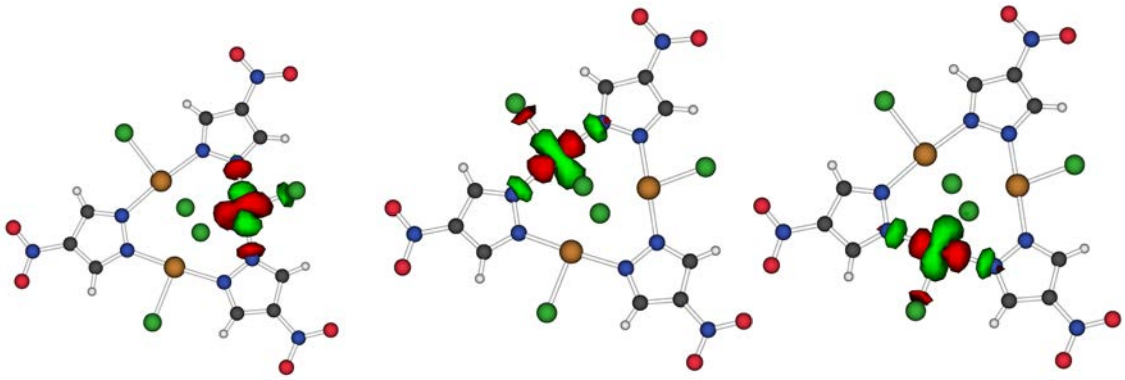

Figure 3. Localized magnetic orbitals of **1** constructed from the CASSCF delocalized MOs. A similar picture holds for **2a** and **2b**.

EPR spectroscopy

Single-crystal studies

To better understand the character of the quartet ground state in **1**, single-crystal EPR studies were undertaken. EPR spectra were characteristic of zfs systems, and they were attributed to the ground S = 3/2 state, in perfect agreement with previously reported CH_2Cl_2 solution EPR spectra.[22] No signals of the excited doublets could be detected even at room temperature, probably due to fast relaxation. The spectra were characterized by broad lines due to unresolved hyperfine interactions. The amplitude of D (~0.1 cm^{-1}) was small enough for the EPR signals to fall nicely within the observable window of X-band EPR wavelength (~0.3 cm^{-1}), thus not necessitating the use of higher frequencies.

Experiments on oriented crystals were complicated by their low symmetry (triclinic $P\ \bar{1}$, one independent molecule per unit cell) and the non-trivial relation between the molecular z-axis and the unit cell axes. Attempts to index single crystals and derive such relations were unsuccessful as the indexed faces could only be assigned to crystallographic planes with high Miller indices. These complications did not allow the confirmation of the absolute orientation of the magnetic z-axis within the crystal and, therefore, with respect to the molecular frame. However, they did allow the assessment of axiality of the EPR spectrum and the relative orientations of the g- and D-tensors.

In particular, it was possible to align a crystal by trial-and error, so that the molecule's magnetic axis was almost parallel to the Zeeman field ($\mathbf{B}_0$), as evidenced by the characteristic evenly-spaced 3-line spectrum. A weak extra resonance at 234 mT at that rotation was assigned to the $|3/2, -3/2\rangle \rightarrow |3/2,$

+1/2⟩ transition. This is not permitted when $z||\mathbf{B}_0$, but acquires a non-zero probability amplitude due to the non-parallel alignment of the magnetic axis to the Zeeman field. Rotations were performed from this orientation at 3° intervals between 0-180° (Figure 4, left), and then the crystal was turned by 90° around the two other orthogonal axes to carry out rotations around them (Figure 4, center and right). Due to this imperfect alignment, each series of rotations actually resulted in narrow precessions of the molecular x^M, y^M, z^M axes around the laboratory rotation axis (x^L), with the magnetic field defining the laboratory z-axis (z^L). These rotations are respectively noted as (a), (b) and (c) in Figure 4.

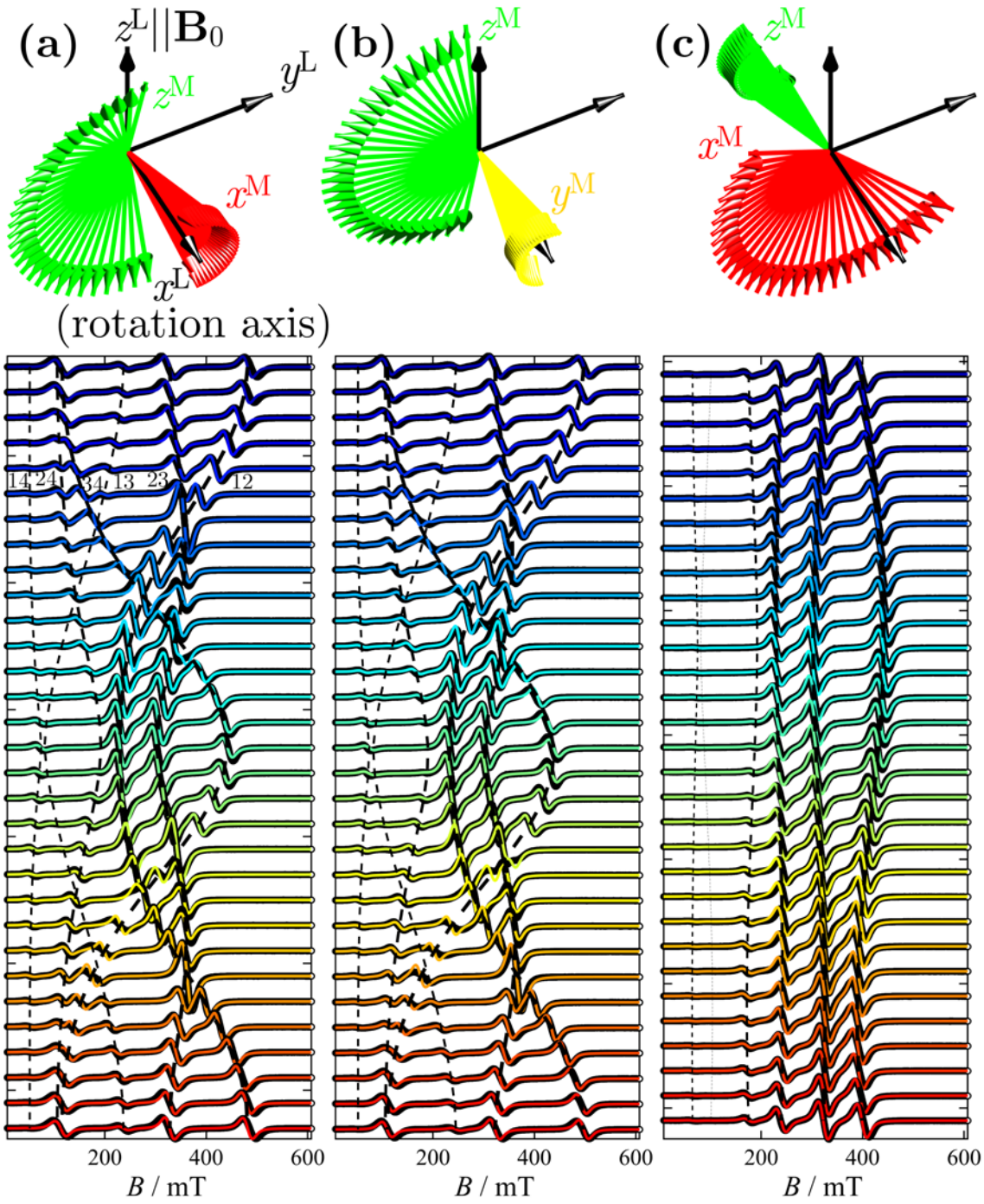

Figure 4. **Top.** Orientations of the molecular *z*-axis during 0-180° rotations **a-c** about the three orthogonal orientations. **Bottom.** Single-crystal X-band EPR spectra of **1** (black points) and their fits (colored lines) according to the models described in the text. For clarity, only every other spectrum is shown. Due to the imperfect alignment of the magnetic *z*-axis to the Zeeman field, the top and bottom spectra in **(a)** and **(b)** are the closest to the ideal evenly spaced 3-line spectrum ($z||\mathbf{B}_0$). Fits to giant-spin and multispin Hamiltonians are visually comparable and the latter are shown (solution **II**). The dashed lines are transition roadmaps, with their thickness indicative of the transition's mean intensity. The

number pairs in panel **(a)** indicate the pairs of states involved in transitions: 1 ≡ |3/2, −3/2⟩, 2 ≡ |3/2, −1/2⟩, 3 ≡ |3/2, +1/2⟩, 4 ≡ |3/2, +3/2⟩. The molecular orientation in the crystal is described by Euler angles {0, 16.0°, 0}. The crystal's initial positions (top of panels) are described by the following Euler angles for each rotation: **(a)**, {0, 0, 0} (by default); **(b)**, {90°, 12.6°, 0}; **(c)**, {0, 90°, 6.0°}. The molecular orientations at those initial positions are described by Euler angles {177.6°, 16.0°, −177.7°}, {82.5°, 12.1°, 3.9°} and {47.5°, 74.7°, -7.6°}, respectively.

Initially the spectra were simulated using the giant-spin approximation, considering a zero-field split $S = 3/2$ system according to the Hamiltonian:

$$\hat{H}_{3/2} = D\hat{S}_z^2 + E(\hat{S}_x^2 - \hat{S}_y^2) + \mu_B \mathbf{H}\tilde{\mathbf{g}}_i\hat{\mathbf{S}}_i \qquad (6)$$

Attempts to fit to an axial (solution **A**) or rhombic (solution **B**) *g*-tensor yielded almost identical results (Table 4). Therefore, the former model was favored to avoid over-parametrization. Consideration of an extremely small rhombicity of the *D*-tensor ($E \sim 8\times10^{-4}$ cm^{-1}, $E/D \sim 0.01$) improved the quality of the fits by ~11% in both cases (solutions **C** and **D**, respectively), a statistically significant improvement for the addition of just one parameter. Considering a small misalignment between the *g*- and *D*-tensors, in particular a relative rotation around the *z*-axis of *ca.* 11-12°, brought about a small (~1.5%) improvement to the fits, considered indicative (see below), though not quantitatively conclusive. Given the low symmetry of the crystal, fits to the giant spin model did not allow us to unequivocally demonstrate the tensor orientations within the crystal and molecular frames. It is reasonably assumed that the g_z and D_{zz} axes are normal to the triangle's plane, an assumption that was confirmed by implementation of the full multispin Hamiltonian analysis (see below).

Table 4. Best-fit parameters to the single-crystal data based on the models described in the text. The *R* factor is Easyspin's RMSD for the same data set.

Solution	g_x (or $g_\parallel$)	g_y	g_z	D (cm^{-1})	E (×10^{-4} cm^{-1})	α_D (°)	R (×10^{-2})
A	2.070	-	2.225	0.107	-	-	4.72
B	2.069	2.070	2.226	0.107	-	-	4.72
C	2.071	-	2.222	0.107	7.95	-	4.19
D	2.069	2.072	2.221	0.107	8.33	-	4.17
E	2.070	-	2.222	0.107	8.47	-11.8	4.13
F	2.069	2.071	2.222	0.107	9.05	-10.7	4.12

Then, EPR spectra were analyzed using the full multispin Hamiltonian to grasp the origin of the zfs. Such Hamiltonian accounts for isotropic, DM, dipolar and anisotropic interactions, as well as for the local g_i-tensor orientations.

To minimize the number of free variables, an isosceles isotropic Hamiltonian term, with $J_{13} = J_{23} = J = -25.9$ cm^{-1} and $J_{12} = J' = -29.1$ cm^{-1} was considered. This assignment was based on the J_{av} value derived from magnetic susceptibility studies ($J_{av} = -27.0$ cm^{-1}, Table 2), and on the ΔJ value derived from consideration of *ab initio* calculations. For that latter parameter, as the calculated J_{av} value exhibited some deviation from the experimentally determined one, the size of ΔJ was calculated by scaling accordingly, and fixed to $|\Delta J_{exp}| = |\Delta J_{calc}| \times (J_{av(exp)}/J_{av(calc)}) = 6.68$ cm^{-1}. As for its sign, which determines the type of isosceles magnetic symmetry ($|J| > |J'|$ *vs.* $|J| < |J'|$), this was determined by the reading of the *ab initio* wavefunctions of doublets D0 and D1, leading to a value of $\Delta J_{exp} = +6.68$ cm^{-1}.

In calculating the dipolar term, the general expression for the interaction matrix was applied, as $\tilde{\mathbf{D}}_{ij}^{dip} = \rho\left[\mathbf{g}_i^{T}\mathbf{g}_j - 3\left(\mathbf{g}_i^{T}\cdot\boldsymbol{\rho}_{ij}\right)\left(\boldsymbol{\rho}_{ij}^{T}\cdot\mathbf{g}_j\right)\right]$ (7), where $\boldsymbol{\rho}_{ij} = \mathbf{r}_{ij}/|\mathbf{r}_{ij}|$ is the unit vector between sites i and j. This is a 3×3 interaction matrix whose structure is a function of the relative orientations of the two g-tensors, and becomes symmetric when they are parallel. In the point-dipole approximation of isotropic spins, it is diagonal and traceless, and the interaction energy is only determined by the intersite distance. This is a satisfactory approximation in the case of organic radicals separated by large distances. However, in the case of highly anisotropic metal ions in close proximity, g-tensor misalignments become important. Analytical expressions have been derived in the reference frame of one of the spins ($\mathbf{g}_1$ by convention, whose tensor is therefore diagonal).[46,47] Whereas this may be a useful convention for dinuclear complexes (or radical pairs), the use of the molecular frame of reference is a more convenient convention for higher nuclearity systems.

We opted for the latter convention and defined the principal axes of the local g-tensors with respect to the molecular frame of reference. In doing so, we took into account the compressed tbp coordination sphere of the copper(II) ions, which gives rise to magnetic orbitals of d_{z^2} character, as already mentioned. This coordination geometry reverses the g-tensor values to $g_\perp > g_\parallel$[56–61] an observation taken into consideration during the fits.

According to the above, we arranged their tensors so that their principal z-axes coincide with the idealized N-Cu-N directions, with the Euler angles $\{\alpha, \beta, \gamma\}$ being $\{\pi, -\pi/2, \gamma_1\}$, $\{-\pi/3, -\pi/2, \gamma_2\}$ and $\{\pi/3, -\pi/2, \gamma_3\}$ for sites $i = 1$, 2 and 3, respectively, with respect to the molecular frame (Figure 5 and Figure 6), where γ_i is the "twist" of the $g_\perp$ axes with respect to the triangle plane (for simplicity, the

convention selected for Euler angles is *zyz'*, as used by *Easyspin* functions). This can intuitively be associated, though it does not strictly coincide (see below), with the angular deviation of the terminal chlorides from the in-plane position. We then calculated the respective rotation matrices $\mathbf{R}(\alpha, \beta, \gamma)$ which transform the tensors to the molecular frame (M-frame) through the relation:

$$\tilde{\mathbf{g}}' = \mathbf{R}(\alpha,\beta,\gamma)\cdot\tilde{\mathbf{g}}\cdot\mathbf{R}^{\mathrm{T}}(\alpha,\beta,\gamma) \qquad (8)$$

We then used $\tilde{\mathbf{g}}'$ to calculate the interaction matrices in the molecular frame. In that frame, the vectors $\boldsymbol{\rho}_{12}$, $\boldsymbol{\rho}_{13}$ and $\boldsymbol{\rho}_{23}$ were described by Euler angles {π/3 0 0}, {-π/3 0 0} and {π/2 0 0}, respectively. Due to the presence of antisymmetric elements in the $\tilde{\mathbf{D}}_{ij}^{dip}$ tensors when expressed in the M-frame, we decomposed them to their symmetric and antisymmetric parts to find their real eigenvalues:

$$\tilde{\mathbf{D}}_{ij}^{dip(sym)} = \left(\tilde{\mathbf{D}}_{ij}^{dip} + (\tilde{\mathbf{D}}_{ij}^{dip})^{T}\right)/2 \qquad (9)$$

$$\tilde{\mathbf{D}}_{ij}^{dip(anti)} = \left(\tilde{\mathbf{D}}_{ij}^{dip} - (\tilde{\mathbf{D}}_{ij}^{dip})^{T}\right)/2 \qquad (10)$$

and used the symmetric part for the plots of $\tilde{\mathbf{D}}_{M}^{dip}$.

A comment should be made regarding the validity of this model. It is known that spin delocalization, *e.g.* such as observed in unsaturated radical systems, can cause important deviations from the point-dipole approximation.[62] In our case, calculations show that orbitals located on the metal centers are of d character and are not delocalized over the molecule. Indeed, the HOMO orbital is antibonding between the metals and the pyrazole nitrogen atoms (Figure 3). Another possible source of deviation from the point-dipole model is the redistribution of spin density due to magnetic exchange, which influences the spin expectation values $\langle\hat{S}_{iz}\rangle$, i.e. the spin density on each site.[40,54] For the spin Hamiltonian parameters of **1**, calculations show that in the ground state $|S_T = 3/2, M_S = -3/2\rangle$, the three spin centers are equivalent, with $\langle\hat{S}_{1z}\rangle = \langle\hat{S}_{2z}\rangle = \langle\hat{S}_{3z}\rangle = -0.5$, which further reinforces the validity of the point-dipole approximation. Similarly, *ab initio* calculations show equal spin densities on the three sites.

Turning to the anisotropic interactions, in the general form of the interaction tensor as expressed in Equation (3), this is defined by five independent variables, *i.e.* $J_{ij}^{\alpha\beta} = J_{ij}^{\beta\alpha}$ (α, β = *x*, *y*, *z*), with $J_{ij}^{zz} = -J_{ij}^{xx} - J_{ij}^{yy}$ being a dependent variable (p. 63 of reference [63]), and its eigenvectors define the reference frame of the pairwise anisotropic exchange interaction. A perfectly equilateral symmetry for this tensor (*i.e.*, $\tilde{\mathbf{D}}_{12}^{ani} = \tilde{\mathbf{D}}_{13}^{ani} = \tilde{\mathbf{D}}_{23}^{ani}$ in the respective frames) introduces an additional consideration: such a model cannot reproduce possible rhombicities stemming from anisotropic interactions, since the tensorial sum cancels them out. Indeed, as was shown on the basis of our numerical simulations, the total $\tilde{\mathbf{D}}_{M}^{ani}$ tensor is then characterized by $J_{M}^{(ani)xx} = J_{M}^{(ani)yy}$, meaning that the coupled ground state

corresponds to a purely axial system, as far as anisotropic exchange is concerned, since ($D_M^{ani} = \frac{1}{2} J_M^{(ani)zz}, E = \frac{1}{2}(J_M^{(ani)xx} - J_M^{(ani)yy})$), even in the presence of rhombic pairwise anisotropic terms (pp. 653-654 of reference [63]).

With such a model, the only rhombicity in the quartet state is due to dipolar interactions, since the r_{ij} distances and γ_i angles (see below) break the structural symmetry. However, it cannot account for rhombicities stemming from anisotropic exchange. One way to circumvent this deficiency, is to relax the constraint of equilateral symmetry in the anisotropic exchange term, introducing 3 × 5 = 15 (instead of just 5) independent variables into the model; However, this leads to overparametrization. To do so with the minimum amount of additional parameters, we initially sought to scale one of the three tensors as $\tilde{\mathbf{D}}_{13,23}^{ani} = a\tilde{\mathbf{D}}_{12}^{ani}$ and use a as a free variable (5 + 1 = 6 free variables). However, this strategy was not successful. Finally, considering $\tilde{\mathbf{D}}_{12}^{ani} \neq \tilde{\mathbf{D}}_{13}^{ani} = \tilde{\mathbf{D}}_{23}^{ani}$ (5 + 5 = 10 free variables), significantly improved the agreement to the data, but due to the important number of additional free variables we remain cautious as to the physical significance of the magnitude of each of these variables.

To summarize, the multispin Hamiltonian matrix considered was:

$$\begin{aligned}\hat{H} = {} & J(\hat{\mathbf{S}}_1 \cdot \hat{\mathbf{S}}_3 + \hat{\mathbf{S}}_2 \cdot \hat{\mathbf{S}}_3) + J'\hat{\mathbf{S}}_1 \cdot \hat{\mathbf{S}}_3 + \sum_{i,j=1}^{3} \mathbf{G}_{ij}(\hat{\mathbf{S}}_i \times \hat{\mathbf{S}}_j) + \\ & + \sum_{i,j=(1,3),(2,3)} \hat{\mathbf{S}}_i \cdot \tilde{\mathbf{D}}_{ij}^{ani} \cdot \hat{\mathbf{S}}_j + \hat{\mathbf{S}}_1 \cdot \tilde{\mathbf{D}}_{12}'^{ani} \cdot \hat{\mathbf{S}}_2 + \sum_{i,j=1}^{3} \frac{\beta^2}{r_{ij}^3} \hat{\mathbf{S}}_i \cdot \tilde{\mathbf{D}}_{ij}^{dip} \cdot \hat{\mathbf{S}}_j + \beta \mathbf{H} \sum_{i=1}^{3} \tilde{\mathbf{g}}_i \hat{\mathbf{S}}_i\end{aligned} \tag{11}$$

but its physical meaning can confidently be established only in the case of $\tilde{\mathbf{D}}'^{ani} = \tilde{\mathbf{D}}^{ani}$.

The crystal structure was used to fix the intermetallic distances and to provide an initial estimate of the *g*-tensor orientations. Only three free variables were introduced in this part of our model, in particular those describing the "twist" of the individual $g_{i\perp}$ axes with respect to the triangle plane. The principal values of the *g*-tensors were considered equal for all three ions, requiring the introduction of only three variables. Five (or ten, see above) variables were considered for the general expression of the anisotropic exchange interactions.

Similarly, three additional variables would be required for DM interactions; although the anions do not contain crystallographically imposed C_3 axes and σ_h planes, the molecular symmetry is such that can be approximated by a pseudo-D_{3h} point group. Following the Moriya rules, this allows to consider G_z as the principal component of the DM interaction matrix. However, these variables were finally discarded, as will be explained (*vide infra*).

In all, eleven (or sixteen) free variables were considered for the Hamiltonian, plus four more to describe the orientation of the molecule in the crystal and of the crystal in the laboratory frame, and two to describe the intrinsic line widths (Gaussian and Lorentzian). These seventeen (or twenty-two) fitting parameters compare quite well with the 183 (= 61 × 3) single-crystal spectra which formed our data set.

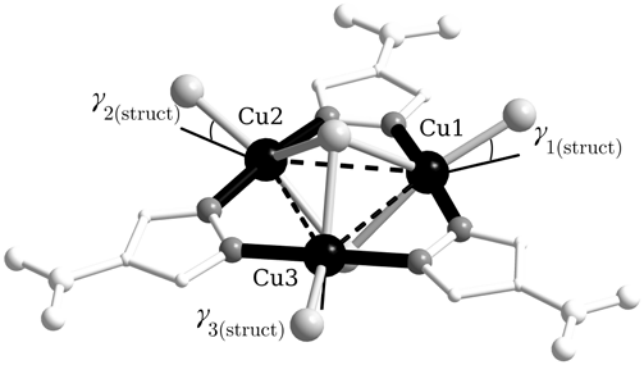

Figure 5. Structure of the anion of **1** showing the intramolecular superexchange interactions (dashed lines). The axial compression axes of the trigonal bipyramids are indicated by black thick bonds, whereas the equatorial planes are indicated by grey thin bonds. The angles $\gamma_{1\text{-}3}$ indicate the deviation of the Cu-Cl_{term} bonds from the triangle plane.

Initial attempts to fit the spectra by only considering the dipolar interactions yielded a partial account of the zfs of the ground state, confirming that DM and/or anisotropic interactions need also be considered. Our first attempt considered DM interactions based on the predictions of Belinsky[29] However, no discernible zfs was induced by any combination of $G_{x/y/z}$ elements. Simulations showed that the only way to introduce zfs through DM interactions was to reverse one of the **G** pseudovectors, i.e. assume that $[G_{12x}\ G_{12y}\ G_{12z}] = [G_{13x}\ G_{13y}\ G_{13z}] = -[G_{23x}\ G_{23y}\ G_{23z}]$ (expressed in the local interaction frames), for which, however, no plausible rationale could be found.

We therefore turned to anisotropic interactions as a zfs-inducing term. A series of fits demonstrated that J_{ij}^{xx} and J_{ij}^{yy} (expressed in the local *ij*-reference frames) were the leading parameters in determining the zfs and that several combinations achieved very good agreement with experimental data. Indicative fits with values of *ca.* -0.045 cm^{-1} are shown on Table 5. The total $\tilde{\mathbf{g}}_M$ and $\tilde{\mathbf{D}}_M^{ani}$ were calculated through the following relations for an S_T = 3/2 state stemming from three S_i = 1/2 spins (Table 4.4 of reference [45]):

$$\tilde{\mathbf{g}}_M = \tfrac{1}{3}\tilde{\mathbf{g}}_1 + \tfrac{1}{3}\tilde{\mathbf{g}}_2 + \tfrac{1}{3}\tilde{\mathbf{g}}_3 \quad (12)$$

and

$$\tilde{\mathbf{D}}_M = \tilde{\mathbf{D}}_M^{ani} + \tilde{\mathbf{D}}_M^{dip} \quad (13)$$

where

$$\tilde{\mathbf{D}}_M^{ani} = \tfrac{1}{6}\tilde{\mathbf{D}}_{12}^{ani} + \tfrac{1}{6}\tilde{\mathbf{D}}_{13}^{ani} + \tfrac{1}{6}\tilde{\mathbf{D}}_{23}^{ani} \quad (14)$$

$$\tilde{\mathbf{D}}_M^{dip} = \tfrac{1}{6}\tilde{\mathbf{D}}_{12}^{dip} + \tfrac{1}{6}\tilde{\mathbf{D}}_{13}^{dip} + \tfrac{1}{6}\tilde{\mathbf{D}}_{23}^{dip} \quad (15)$$

and where each individual tensor is expressed in the M-frame for the addition.

The various models tested indicate that a ~10% improvement to the fit quality was obtained by introducing the rotations of the local g_i-tensors as free variables (solution **II**). Additionally, breaking the equilateral symmetry of the anisotropic interactions by introducing an independent $\tilde{\mathbf{D}}_{12}^{ani}$ interaction matrix (solution **III**) affords a further improvement of ~11% over solution **II**. Although this is to be statistically expected from the introduction of five free variables, we note that this solution better reproduces the rhombic zfs term that was found during fits to the giant spin model (see Table 4).

Figure 6 shows the orientations of the various tensors for solution **II** of Table 5, in the reference frames in which each is diagonal. It should be noted that these tensors are not diagonal in the same reference frames, and that their principal axes (eigenvectors) do not perfectly coincide with any of the *M* and *ij* frames. For comparison, the respective plots for solutions **I** (Figures S1) and **III** (Figure S2) are given in the Supporting Information.

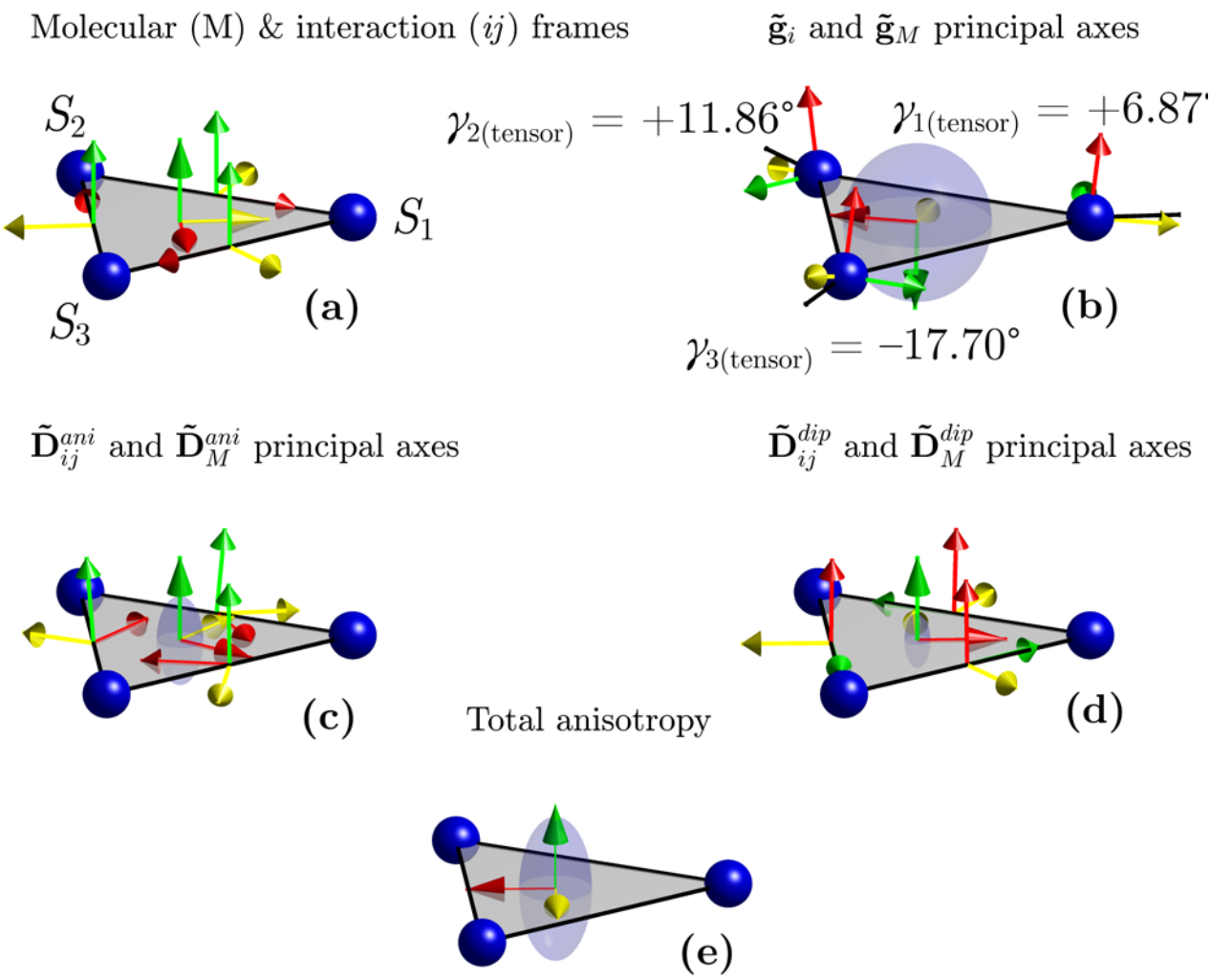

Figure 6. Illustration of tensor elements based on best-fit parameters of solution **II** (axis color code: *x* = red, *y* = yellow, *z* = green). **(a).** Principal reference frames definitions: molecular (M) on the triangle center, and interaction (*ij*) on the midpoints of the interspin vectors. **(b-d).** Principal axes of local and molecular *g*-tensors **(b)**, local and molecular anisotropic exchange tensors **(c)** and dipolar interaction tensors **(d)** as determined from fits to single-crystal data. **(e).** Local axes of the total anisotropy tensor derived from the sum of the anisotropic and dipolar parts. The blue semi-transparent ellipsoids illustrate the relative sizes of the eigenvalues along each axis, hence the axiality of each tensor. For $\tilde{\mathbf{D}}_M^{ani}, \tilde{\mathbf{D}}_M^{dip}, \tilde{\mathbf{D}}_M$ they are in the same scale.

These results are in very good agreement with the fits carried out based on a giant-spin model. They corroborate our initial assumption that the principal *z*-components of **g** and **D** axes are normal to the triangle plane and practically collinear, with a misalignment mainly regarding a rotation around their common *z*-axis.

Our results indicate an almost axial *g*-tensor, and reproduce faithfully the results of the giant-spin solution **C**. They also yield an average *g* value $g_{av} = \sqrt{(g_x^2 + g_y^2 + g_z^2)/3}$ = 2.124, *i.e.* remarkably close to the value of 2.125 derived from magnetic susceptibility data (Table 2). They also rationalize the fact that although the local *g*-tensors have an inversed order ($g_{i\|} < g_{i\perp}$) the coupled system exhibits a "normal" order for Cu^{II} ($g_{M\|} > g_{M\perp}$). Indeed, as the local (large) g_x components are projected onto the molecular *z*-axis, they yield a large g_{zM} due to their out-of-plane orientations. As far as the "twist" angles are concerned, the fits showed a remarkable sensitivity to the values of these parameters, and a clear preference for a particular local error minimum. We should note, however, that these angles do not coincide with any structural parameters, the most intuitive of which would be the angular deviation of the $Cu\text{-}Cl_{terminal}$ bond out the Cu_3 plane. The only empirical correlation we established is that the local *g*-tensors are rotated around their *z*-axes by *ca.* 15-30° with respect to the $Cu\text{-}Cl_{terminal}$ bond (see $\gamma_{i(struct)} - \gamma_{i(tensor)}$ in Table 6).

The two series of fits (giant-spin *vs* multispin model) are also coherent with respect to the improvement brought about by full inclusion of rhombic contributions of anisotropic exchange, as they closely reproduce the sizes of *D* and *E* of the ground state zfs. The non-uniqueness of solutions for anisotropic interactions is attributed to the triangular symmetry of the system which results in different parameter sets yielding similar tensorial sums.

Table 5. Best-fit parameters according to different models and derived parameters of the coupled-system tensors. The different solutions illustrate the effect of inclusion of *g*-tensor rotations and of an isosceles distortion of the anisotropic exchange to the quality of the fits. Figures in bold italics indicate fixed values.

	I	**II**	**III**[b]
Multispin Hamiltonian best-fit parameters			
J_{ij}^{xx} (cm^{-1})	−0.0453	−0.0452	−0.0447, −0.0481
J_{ij}^{yy} (cm^{-1})	−0.0439	−0.0436	−0.0448, −0.0403
$J_{ij}^{zz} (= -J_{ij}^{xx} - J_{ij}^{yy})$ (cm^{-1})[a]	0.0892	0.0888	0.0895, 0.0884
J_{ij}^{xy} (cm^{-1})	0.00969	0.00942	0.0107, 0.00938
J_{ij}^{xz} (cm^{-1})	0.00953	0.00836	0.00844, 0.00767

J_{ij}^{yz} (cm^{-1})	0.00867	0.00909	0.00941, 0.00897
g_{ix}	2.226	2.226	2.225
g_{iy}	2.126	2.126	2.125
g_{iz}	2.014	2.015	2.013
γ_1 (°)	***0***	6.87	9.25
γ_2 (°)	***0***	11.86	11.82
γ_3 (°)	***0***	−17.70	−23.36
RMSD	4.35×10^{-2}	3.90×10^{-2}	3.49×10^{-2}
Derived spin-Hamiltonian parameters for exchange-coupled quartet state			
D^{ani}, E^{ani} (cm^{-1})	0.0670, 0	0.0666, 0	0.0667, -7.17×10^{-4}
D^{dip}, E^{dip} (cm^{-1})	0.0410, -5.09×10^{-4}	0.0408, -4.83×10^{-4}	0.0406, -4.72×10^{-4}
D^{tot}, E^{tot} (cm^{-1})	0.108, -5.09×10^{-4}	0.107, -4.83×10^{-4}	0.107, -1.12×10^{-3}
g_{Mx}	2.070	2.072	2.071
g_{My}	2.070	2.072	2.073
g_{Mz}	2.227	2.223	2.220

[a]Dependent variable. [b]Double values for the anisotropic exchange parameters refer to tensor elements $J_{13,23}^{\alpha\beta}$, $J_{12}^{\alpha\beta}$ ($\alpha, \beta = x, y, z$).

Table 6. Comparison between the out-of-plane deviation of the terminal chlorides with the "twist" angle of the local g_i-tensors around the g_{iz} local axes (from solution **II**).

i-ion	$\gamma_{i(\text{struct})}$ (°)	$\gamma_{i(\text{tensor})}$ (°)	$\gamma_{\text{struct}} - \gamma_{\text{tensor}}$ (°)
1	−21.01	+6.87	−27.88
2	−19.67	+11.86	−31.53
3	+0.64	−17.70	+17.06

A final comment is in order regarding the signs of *D* and *E*: During the fitting attempts, simulations were carried out on an extensive number of parameter combinations for the anisotropic exchange interaction matrix. Of all these combinations, none led to a negative value of *D* after eigendecomposition. On the one hand, this is in agreement with the findings of high-frequency EPR studies previously reported on the related complex $(Bu_4N)_2[Cu_3(\mu_3\text{-}Cl)_2(pz)_3Cl_3]$, and which concluded that $D > 0$.[23] On the other hand, the present simulations may also point towards the conclusion that the

symmetry of the problem does not allow for $D < 0$, at least when dipolar and anisotropic interactions are considered. A mathematical proof to that effect is beyond the scope of the current work, so, this conclusion is offered on a tentative basis.

With regard to the sign of E, this is determined during the diagonalization of the full interaction matrix $\mathbf{J} = \sum_{i,j=1}^{3} \tilde{\mathbf{D}}_{ij}^{HDvV} + \tilde{\mathbf{D}}_{ij}^{DMI} + \tilde{\mathbf{D}}_{ij}^{ani} + \frac{\beta^2}{r_{ij}^3}\tilde{\mathbf{D}}_{ij}^{dip}$, whose individual terms are given Equations 1-4 and 7. The order of eigenvalues in the diagonalized matrix $\mathbf{D} = \mathbf{V}^T\mathbf{J}\mathbf{V}$ is related to the ordering of matrix $\mathbf{V}$ containing the eigenvectors as columns. By choosing an ascending order ($D_{xx} < D_{yy} < D_{zz}$), the x and y eigenvectors in $\mathbf{V}$ may be swapped in low rhombicity ($D_{xx} \sim D_{yy}$) systems. This a typical situation in zfs systems, where the sign of E bears no physical meaning, other than signifying the handedness of the reference frame.

Powder and solution EPR spectra

Single-crystal EPR data are not always easily available, nor is their analysis always straightforward. We were therefore interested to assess whether we could derive useful conclusions as to the magnetic structures of ferromagnetic Cu^{II}_3 pyrazolates from powder or frozen solution data. Accordingly, EPR spectra were collected from powders and frozen CH_2Cl_2 solutions of **1-4**.

Powder spectra of complexes **1**, **2** and **4** exhibited characteristic zfs spectra, attributed to their S = 3/2 ground states. Preliminary fits with a simple giant-spin model yielded excellent results assuming collinear **g** and **D**, with solid-state g_{av} values for **1-3** (2.121, 2.164, 2.115, respectively, Table 7) following closely the ones determined from magnetic susceptibility data, even reproducing the higher *g-value* of **2** (Table 2). These fits revealed consistent D values of *ca.* 0.08-0.11 cm^{-1} in the solid state and 0.04-0.1 cm^{-1} in frozen solutions. Except for the powder spectrum of **1**, all other spectra required the introduction of small D-strains to satisfactorily fit the data, using Easyspin's built-in function. This is attributed to distributions of magnetic conformers for the frozen solution spectra, and to the presence of more than one molecules in the asymmetric units of **2** and **3** (two and four, respectively) in the solid state spectra.

A salient exception was the low-melting[24] **3**, which was characterized by an exceptionally small zfs and broad lines which masked the characteristic zfs patterns, particularly for a molten and re-cooled frozen glass. For that particular spectrum, the smearing out of any distinctive patterns precluded any meaningful fit, and only a tentative simulation was carried out. In turn, the frozen solution spectrum was characterized by somewhat narrower lines, which allowed simulation taking into account a Gaussian distribution of the D parameter. This was the lowest among the complexes studied here. In the

context of the giant spin analysis, a custom-made *D*-strain model was applied, considering a combination of Gaussian and Lorentzian distributions of the *D* parameter, as previously implemented in other systems.[64,65]

Table 7. Best-fit parameters from fits of powder and frozen solution EPR spectra of complexes **1**-**4** to a giant-spin model. The $\sigma_{G/L}$ values are the Gaussian and Lorentzian contributions to the intrinsic line widths, and σD_G is the Gaussian line width of the *D*-strain.

Complex	State	*T* / K	$\lvert D\rvert$ (cm^{-1})	$g_{\parallel}$	$g_{\perp}$	σ_G/σ_L (mT)	σD_G (cm^{-1})	g_{av}
1	Powder	290	0.105	2.213	2.074	25.4/0	0	2.121
	CH_2Cl_2	4.2	0.096	2.212	2.085	21.0/0	0.043	2.128
2	Powder	290	0.079	2.290	2.098	30/14	0.041	2.164
	CH_2Cl_2	4.2	0.050	2.190	2.088	17.7/0	0.017	2.123
3	Powder	290	0.037	2.222	2.060	20/20	0	2.115
	Molten	290	~0	~2.10	~2.10	0/50		
	CH_2Cl_2	4.2	0.043	2.247	2.088	14.6/6.8	0.033/0.017	2.142
4	Powder	290	0.088	2.226	2.080	37.8/0	0.035	2.130
	CH_2Cl_2	4.2	0.059	2.185	2.091	17.5/0	0.040	2.123

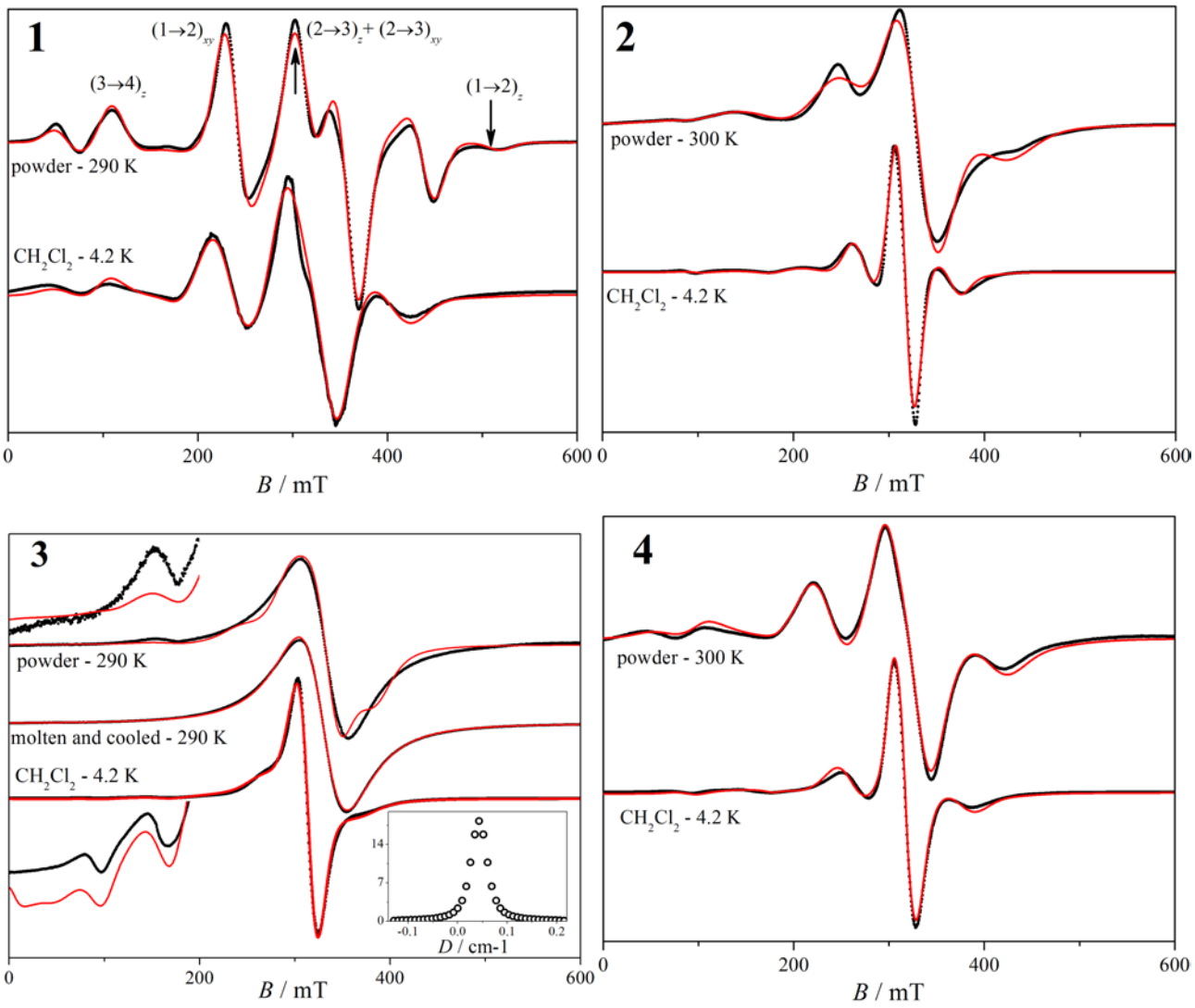

Figure 7. Powder (290 K) and frozen CH_2Cl_2 solution (4.2 K) X-band EPR spectra of **1**-**4** and fits based on a giant-spin Hamiltonian, assuming axial zfs and *D*-strain effects. The *D*-strain effect for the frozen solution spectrum of complex **3** was carried out using a custom distribution function, shown in the inset.

Subsequently, we attempted to interpret our powder and solution data with a simplified version of the previously employed multispin Hamiltonian. In particular, we considered axial local *g*-tensors and, accordingly, we neglected their "twist" angles. Moreover, we neglected the pairwise rhombicities of anisotropic interactions by considering a minimal form of the anisotropic exchange interaction matrix:

$$\tilde{\mathbf{D}}_{ij}^{ani} = J_{ij}^{zz}\begin{bmatrix} -1/2 & 0 & 0 \\ 0 & -1/2 & 0 \\ 0 & 0 & 1 \end{bmatrix} \qquad (16)$$

According to our methodology, dipolar interactions were calculated from structural parameters appropriate to this level of precision, namely the r_{ij} distances, since the *g*-tensor orientations were considered indeterminate from powder data. This cautious approach was validated by the subsequent observation that even the $g_{i\parallel}$ and $g_{i\perp}$ values were indeterminate in some data sets, obliging us to constrain them to physically meaningful values for copper(II) ions (*i.e.* $g_i > 2$). The results of the fits are summarized in Table 8.

During our fitting attempts of the powder data of **1**, we observed that two solutions give good fits, one with $J^{zz} \sim +0.085$ cm^{-1}, and another with $J^{zz} \sim -0.19$ cm^{-1}. However, eigenvalue analysis revealed that the latter corresponds to physically non-meaningful parameters with $E/D \sim 1$, whereas eigenvector analysis indicates that in that solution the principal anisotropy axis lies in the triangle plane (Figure S3). This solution was therefore discarded, while that observation was then used to assess subsequent fits to the data of the other complexes. The results for **1** were in close agreement with the single-crystal fits, yielding practically the same J^{zz} parameter, thus validating our methodology (*cf.* Table 5 and Table 8).

Globally, fits for all complexes were of good quality (Figure 9), although somewhat inferior to that of the fits to a giant-spin model (Figure 7) as we did not consider strain effects. Moreover, the derived *D* parameters for the exchange-coupled quartets were very close to the ones derived from the giant-spin model (*cf.* Table 7 and Table 8). Taken together, these observations further validated our approach. It should also be noted that the dipolar contributions to zfs all fell within a very narrow range (0.038-0.039 cm^{-1}), to be expected from the very similar structures of the complexes.

Table 8. Best-fits parameters to the powder EPR spectra of complexes **1**-**4** using the simplified version of the full multispin Hamiltonian. [a] Figures in bold italics indicate fixed values.

Complex	**Multispin Hamiltonian parameters**				**Derived parameters for quartet-state**					
	$g_{i\parallel}$	$g_{i\perp}$	σ_G/σ_L (mT)	J^{zz} (cm^{-1})	D^{dip} (cm^{-1})	D^{ani} (cm^{-1})	D (cm^{-1})	$g_{M\parallel}$	$g_{M\perp}$	D^{ani}/D (%)

1	***2.001***	2.178	15.8/10.4	0.0850	0.0393	0.0637	0.103	2.181	2.091	62
2a[b]	2.071	2.179	18.9/25.3	0.0481	0.0380	0.0360	0.0741	2.179	2.125	49
2b[b]	2.071	2.179	18.9/25.3	0.0479	0.0382	0.0359	0.0741	2.179	2.125	49
3[c]	2.092	2.155	24.3/0	***0***	0.0387	0	0.0387	2.155	2.123	0
4[d]	***2.001***	2.161	25.3/14/8	0.0663	0.0388	0.0497	0.0885	2.166	2.084	56

[a]Values of $J_{av(exp)}$ and $\Delta J_{\text{“exp”}}$ for **1**, **2a** and **2b** taken from Table 3. In the absence of calculations for **3** and **4**, the values of **1** were used. [b]Dipolar contributions calculated using r_{ij} distances of the respective molecule. [c]Frozen solution spectrum (CH_2Cl_2, 4.2 K), assuming $r_{12} = r_{13} = r_{23} = 3.4$ Å. [d]There are four molecules in the asymmetric unit and for simplicity calculations assume a single molecule with $r_{12} = r_{13} = r_{23} = 3.4$ Å.

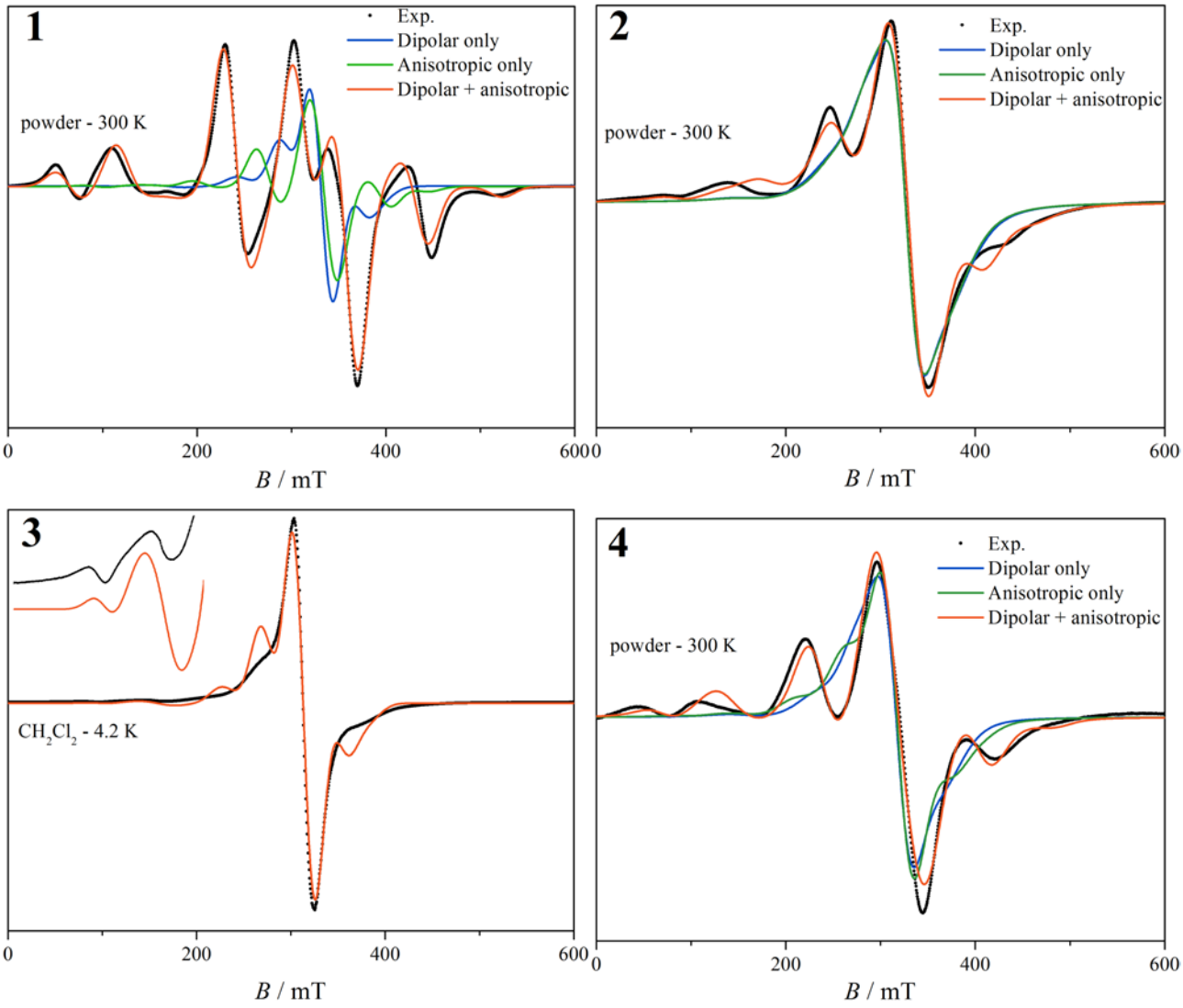

Figure 8. Fits based on the simplified multispin Hamiltonian model described in the text, showing hypothetical spectra accounting for the dipolar-only and anisotropic-only anisotropies. Calculated spectra do not consider any strain effects. For **1**, **2** and **4** powder spectra are shown. For **3** the frozen CH_2Cl_2 spectrum is shown and only the dipolar part is calculated. The inset in that spectrum is a magnification of the low-field region.

An interesting body of conclusions derived from this treatment regards the fraction of zfs induced by dipolar interactions in comparison with that induced by anisotropic exchange. Whereas the anisotropic contribution was around 50-60% for complexes **1**, **2** and **4**, it was practically nil for **3**, whose dipolar term was sufficient to account for its zfs. Indeed, setting $J^{zz} \sim 0$ the dipolar interactions can reasonably reproduce the positions of the features of the frozen solution spectrum. The broadening of the features of the spectrum was not fully accounted for by this monodisperse model, which confirmed the interplay of strain effects previously detected using the giant-spin model. Assuming that dipolar interactions are the sole source of zfs in **3**, the corresponding distributions should therefore be attributed to the presence of a series of structural conformers with a distribution of dipolar interactions.

As a general observation, our method is shown to be applicable in the analysis of even powder or frozen solution spectra. Indeed, considering only the interionic distances and the orientation of the principal *g*-tensor axis, we were able to nicely reproduce the magnitude of the anisotropic exchange derived from the single-crystal data of **1**. Applying this method to complex **3**, we determined that, at variance with the other complexes, it is characterized by negligible anisotropic interactions, although the structural parameters are similar to **1**, **2** and **4**. Given these structural similarities, we lack a valid explanation as to this difference, since theoretical models are based on structural data as their key input. Moreover, electronic effects induced by the pyrazolato side groups are similarly excluded, since complex **2** containing unsubstituted pyrazoles, exhibits EPR spectra similar to the complexes with 4-NO_2- (**1**) and 4-Ph- (**4**) substituted pyrazoles.

The final synthetic variable that has not been examined is the counterion since, on an intuitive level, it is not expected to exert any effect other than modulating the crystal packing in the solid state. This might eventually induce weak structural effects within the molecule, but they would in any case be measurable by X-ray crystallography. What is more, counterions are expected to play an even weaker role in solution assuming they are further removed from the complex molecules.

However, the fact that the $bmim^+$ cations have the special property of favoring the development of ionic liquids, their role becomes intriguing, particularly considering that solutions of magnetic ionic

liquids have exhibited micellar structures[66–68] In fact, this behavior is reminiscent of a "counterion effect" we detected in frozen solutions of two twelve-membered series of "basic" iron(III) carboxylates, containing perchlorates and nitrates as counteranions (24 complexes in total). Using ^{57}Fe Mössbauer spectroscopy, we had detected very distinctive modulations of their quadrupole splittings.[69] Very recently, such a trend has been noted from pulsed EPR studies of a series of salts of V^{IV} anionic complexes comporting different countercations.[60] It is noteworthy that in both cases, the techniques that allowed the identification of such minor effects can probe extremely small energy differences (e.g. from 10^{-3} cm^{-1} in the case of Mössbauer to 10^{-2} cm^{-1} in the case of EPR). Such differences remain highly challenging even for modern theoretical tools, particularly considering that they may involve large ensembles of molecules.

Conclusions

Magnetic susceptibility studies have confirmed the propensity of pyrazolato-bridged complexes containing the $\{Cu_3(\mu_3\text{-}Cl)_2(\mu\text{-}pz)_3\}^+$ core to exhibit ferromagnetic interactions and X-band EPR studies revealed that their ground S = 3/2 state is characterized by a small but discernible zfs. In this work, we focused on the origins of the ferromagnetism and magnetic anisotropy observed in these complexes, attempting to rationalize the former and derive quantitative estimates of the parameters that define the latter. To achieve that goal, we combined single-crystal EPR studies and *ab initio* calculations.

In particular, we ascertained that the magnetic exchange between the copper ions in a compressed tbp coordination, takes place through their d_{z^2} orbitals. Consequently, their ferromagnetic exchange is better rationalized, counterintuitively, through their inefficient overlap with the orbitals of the pyrazolato ligands (a three-bond path), rather than the Cu-Cl-Cu angles with the bridging chlorides (a two-bond path).

In analyzing the parameters that determine the ground state anisotropy, we considered that this could only be brought about through pairwise interaction terms, since for the S = 1/2 Cu^{II} ions no such single-ion term is defined. We therefore constructed a multispin Hamiltonian accounting for all exchange interaction terms (isotropic, antisymmetric, anisotropic) as well as for dipolar interactions. This model was then employed in the analysis of single-crystal data of complex **1**. The results of this full analysis revealed that dipolar interactions account for about 40% of the anisotropy of the ground state, the rest being due to exchange interactions.

Turning to those interactions, we tested both DM (antisymmetric) and anisotropic exchange terms in order to derive a description of the anisotropy-inducing terms. We concluded that DMI could, in

principle, induce a zfs in the S = 3/2 state, but only when fixing one of the **G** pseudovectors to an opposite orientation than the other two, *i.e.* considering $\mathbf{G}_{12} = \mathbf{G}_{13} = -\mathbf{G}_{23}$ (expressed in the local interaction frames). We therefore focused on the role of anisotropic exchange in inducing zfs and derived the description of an interaction tensor that accounts for the other 60% of the ground-state zfs.

During the above-mentioned treatment, particular care was given to the description of the *g*-tensors, as their precise orientations influence the dipolar-induced anisotropy. The benefit of this influence was that the tensor principal axes could be determined through fits to single-crystal data. Thus, we were therefore able to ascertain that their *z*-axes were aligned with the N-Cu-N axes and that their *x*- and *y*-axes could not be aligned to any particular bond. Instead, we found that they exhibited a 15-30° deviation from the Cu-Cl_{term} bond directions. Quantitatively, our results confirmed the trend demonstrated in mononuclear complexes for compressed tbp Cu^{II} ions to exhibit inversed *g* values, i.e. $g_z < g_x, g_y$.

We then extended this multispin Hamiltonian approach to the treatment of powder/solution EPR spectra. We first validated this approach by treatment of the powder data of **1** and comparison with the results from single-crystal studies. Having established its validity, we applied this methodology to the spectra of the other complexes, which allowed us to carry out comparisons within the family of **1-4**. These comparative studies revealed the atypical behavior of **3**, whose anisotropic-exchange component is practically zero, both in the solid state and in solution. This notable exception does not correlate with the nature of the pyrazolato ring peripheral substitution, as complex **2,** which bears the same unsubstituted ligand as **3**, exhibits the same zfs as **1** (4-NO_2) and **4** (4-Ph). By observing that **3** contains $bmim^+$ counterions, principally known for their propensity to induce the formation of ionic liquids, we are tentatively led to consider the possibility of a counterion influence in fine-tuning the magnetic structures of these complexes, both in the solid state and in solution. We have previously noted such counterion effects in a ^{57}Fe Mössbauer study of frozen solutions of Fe^{III} carboxylate triangles[69] whereas similar conclusions have been derived from pulsed EPR.[70] This emerging trend suggests that such a counterion effect may be a general phenomenon in solutions of magnetic metal complexes, and one that merits further study. Although this is beyond the scope of this work, we suggest that the methodology we employ for the detailed description of the magnetic structures of polynuclear systems may enhance our ability to detect such minor effects from spectroscopic data.

As a final methodological conclusion, we showed that when $S > 1/2$ magnetic states of polynuclear complexes are spectroscopically observable, EPR spectroscopy in combination with magnetic and theoretical studies, can provide very precise information on finer terms of their spin Hamiltonians, once

dipolar terms have been properly accounted for. While this approach is realistically applicable even on powder or solution data, its power increases when single-crystal EPR data are available.

Acknowledgments

The authors thank Dr. Yiannis Sanakis for preliminary measurements and helpful discussions, Dr. David I. Kreiger for the single crystal of **4**, and Prof. Philippe Turek for support throughout this study. This project has received funding from the European Union's Horizon 2020 research and innovation programme under the Marie Sklodowska-Curie grant agreement No 746060 (project "CHIRALQUBIT"), by the Fondation pour la Recherche en Chimie (Strasbourg) under the Innovation grant agreement PTu-FRC-0003 (project "MiSSTri") and the National Science Foundation (CHE-1213683).

Supporting information

Materials and methods, and tensor representations. Structural description and crystal structure parameters for complex **4**. CCDC-1986254 contains the supplementary crystallographic data for this complex. These data can be obtained free of charge from the Cambridge Crystallographic Data Centre via www.ccdc.cam.ac.uk/data_request/cif.

Conflict of interest

The authors have no conflict of interest to declare.

References

(1) Kambe, K. On the Paramagnetic Susceptibilities of Some Polynuclear Complex Salts. *J. Phys. Soc. Jpn.* **1950**, *5* (1), 48–51. https://doi.org/10.1143/JPSJ.5.48.

(2) Guigliarelli, B.; Gayda, J. P.; Bertrand, P.; More, C. Relationship between Structural and Magnetic Properties of the 3Fe Clusters in Iron-Sulfur Proteins. *Biochim. Biophys. Acta BBA - Protein Struct. Mol. Enzymol.* **1986**, *871* (2), 149–155. https://doi.org/10.1016/0167-4838(86)90168-8.

(3) Sanakis, Y.; Macedo, A. L.; Moura, I.; Moura, J. J. G.; Papaefthymiou, V.; Münck, E. Evidence for Antisymmetric Exchange in Cuboidal [3Fe−4S] $^{+}$ Clusters. *J. Am. Chem. Soc.* **2000**, *122* (48), 11855–11863. https://doi.org/10.1021/ja002658i.

(4) Nguyen, H.-H. T.; Nakagawa, K. H.; Hedman, B.; Elliott, S. J.; Lidstrom, M. E.; Hodgson, K. O.; Chan, S. I. X-Ray Absorption and EPR Studies on the Copper Ions Associated with the Particulate Methane Monooxygenase from *Methylococcus Capsulatus* (Bath). Cu(I) Ions and Their Implications. *J. Am. Chem. Soc.* **1996**, *118* (50), 12766–12776. https://doi.org/10.1021/ja961778g.

(5) Hung, S.-C.; Chen, C.-L.; Chen, K. H.-C.; Yu, S. S.-F.; Chan, S. I. The Catalytic Copper Clusters of the Particulate Methane Monooxygenase from Methanotrophic Bacteria: Electron Paramagnetic Resonance Spectral Simulations. *J. Chin. Chem. Soc.* **2004**, *51* (5B), 1229–1244. https://doi.org/10.1002/jccs.200400179.

(6) Chan, S. I.; Wang, V. C.-C.; Lai, J. C.-H.; Yu, S. S.-F.; Chen, P. P.-Y.; Chen, K. H.-C.; Chen, C.-L.; Chan, M. K. Redox Potentiometry Studies of Particulate Methane Monooxygenase: Support for a Trinuclear Copper Cluster Active Site. *Angew. Chem. Int. Ed.* **2007**, *46* (12), 1992–1994. https://doi.org/10.1002/anie.200604647.

(7) Chan, S. I.; Yu, S. S.-F. Controlled Oxidation of Hydrocarbons by the Membrane-Bound Methane Monooxygenase: The Case for a Tricopper Cluster. *Acc. Chem. Res.* **2008**, *41* (8), 969–979. https://doi.org/10.1021/ar700277n.

(8) Chan, S. I.; Lu, Y.-J.; Nagababu, P.; Maji, S.; Hung, M.-C.; Lee, M. M.; Hsu, I.-J.; Minh, P. D.; Lai, J. C.-H.; Ng, K. Y.; Ramalingam, S.; Yu, S. S.-F.; Chan, M. K. Efficient Oxidation of Methane to Methanol by Dioxygen Mediated by Tricopper Clusters. *Angew. Chem. Int. Ed.* **2013**, *52* (13), 3731–3735. https://doi.org/10.1002/anie.201209846.

(9) Shi, K.; Mathivathanan, L.; Boudalis, A. K.; Turek, P.; Chakraborty, I.; Raptis, R. G. Nitrite Reduction by Trinuclear Copper Pyrazolate Complexes: An Example of a Catalytic, Synthetic Polynuclear NO Releasing System. *Inorg. Chem.* **2019**, *58* (11), 7537–7544. https://doi.org/10.1021/acs.inorgchem.9b00748.

(10) Trif, M.; Troiani, F.; Stepanenko, D.; Loss, D. Spin-Electric Coupling in Molecular Magnets. *Phys. Rev. Lett.* **2008**, *101* (21), 217201. https://doi.org/10.1103/PhysRevLett.101.217201.

(11) Trif, M.; Troiani, F.; Stepanenko, D.; Loss, D. Spin Electric Effects in Molecular Antiferromagnets. *Phys. Rev. B* **2010**, *82* (4), 045429. https://doi.org/10.1103/PhysRevB.82.045429.

(12) Troiani, F.; Stepanenko, D.; Loss, D. Hyperfine-Induced Decoherence in Triangular Spin-Cluster Qubits. *Phys. Rev. B* **2012**, *86* (16), 161409(R). https://doi.org/10.1103/PhysRevB.86.161409.

(13) Boudalis, A. K.; Robert, J.; Turek, P. First Demonstration of Magnetoelectric Coupling in a Polynuclear Molecular Nanomagnet: Single-Crystal EPR Studies of $[Fe_3O(O_2CPh)_6(Py)_3]ClO_4 \cdot py$ under Static Electric Fields. *Chem. - Eur. J.* **2018**, *24* (56), 14896–14900. https://doi.org/10.1002/chem.201803038.

(14) Liu, J.; Mrozek, J.; Myers, W. K.; Timco, G. A.; Winpenny, R. E. P.; Kintzel, B.; Plass, W.; Ardavan, A. Electric Field Control of Spins in Molecular Magnets. *Phys. Rev. Lett.* **2019**, *122* (3), 037202. https://doi.org/10.1103/PhysRevLett.122.037202.

(15) Robert, J.; Parizel, N.; Turek, P.; Boudalis, A. K. Polyanisotropic Magnetoelectric Coupling in an Electrically Controlled Molecular Spin Qubit. *J. Am. Chem. Soc.* **2019**. https://doi.org/10.1021/jacs.9b09101.

(16) Abbati, G. L.; Brunel, L.-C.; Casalta, H.; Cornia, A.; Fabretti, A. C.; Gatteschi, D.; Hassan, A. K.; Jansen, A. G. M.; Maniero, A. L.; Pardi, L.; Paulsen, C.; Segre, U. Single-Ion versus Dipolar Origin of the Magnetic Anisotropy in Iron(III)-Oxo Clusters: A Case Study. *Chemistry* **2001**, *7* (8), 1796–1807. https://doi.org/10.1002/1521-3765(20010417)7:8<1796::AID-CHEM17960>3.0.CO;2-Y.

(17) van Slageren, J.; Sessoli, R.; Gatteschi, D.; Smith, A. A.; Helliwell, M.; Winpenny, R. E. P.; Cornia, A.; Barra, A.-L.; Jansen, A. G. M.; Rentschler, E.; Timco, G. A. Magnetic Anisotropy of the Antiferromagnetic Ring [Cr8F8Piv16]. *Chem. - Eur. J.* **2002**, *8* (1), 277–285. https://doi.org/10.1002/1521-3765(20020104)8:1<277::AID-CHEM277>3.0.CO;2-D.

(18) Collison, D.; Murrie, M.; Oganesyan, V. S.; Piligkos, S.; Poolton, N. R. J.; Rajaraman, G.; Smith, G. M.; Thomson, A. J.; Timko, G. A.; Wernsdorfer, W.; Winpenny, R. E. P.; McInnes, E. J. L. Magnetic and Optical Studies on an $S = 6$ Ground-State Cluster $[Cr_{12}O_9(OH)_3(O_2CCMe_3)_{15}]$: Determination of, and the Relationship Between, Single-Ion and Cluster Spin Hamiltonian Parameters. *Inorg. Chem.* **2003**, *42* (17), 5293–5303. https://doi.org/10.1021/ic034541b.

(19) ter Heerdt, P.; Stefan, M.; Goovaerts, E.; Caneschi, A.; Cornia, A. Single-Ion and Molecular Contributions to the Zero-Field Splitting in an Iron(III)-Oxo Dimer Studied by Single Crystal W-Band EPR. *J. Magn. Reson.* **2006**, *179* (1), 29–37. https://doi.org/10.1016/j.jmr.2005.10.016.

(20) Angaridis, P. A.; Baran, P.; Boča, R.; Cervantes-Lee, F.; Haase, W.; Mezei, G.; Raptis, R. G.; Werner, R. Synthesis and Structural Characterization of Trinuclear Cu^{II}–Pyrazolato Complexes Containing μ_3-OH, μ_3-O, and μ_3-Cl Ligands. Magnetic Susceptibility Study of $[PPN]_2[(\mu_3\text{-}O)Cu_3(\mu\text{-}Pz)_3Cl_3]$. *Inorg. Chem.* **2002**, *41* (8), 2219–2228. https://doi.org/10.1021/ic010670l.

(21) Boča, R.; Dlháň, L.; Mezei, G.; Ortiz-Pérez, T.; Raptis, R. G.; Telser, J. Triangular, Ferromagnetically-Coupled Cu^{II}_3–Pyrazolato Complexes as Possible Models of Particulate Methane Monooxygenase (PMMO). *Inorg. Chem.* **2003**, *42* (19), 5801–5803. https://doi.org/10.1021/ic0344416.

(22) Mezei, G.; Raptis, R. G.; Telser, J. Trinuclear, Antiferromagnetically Coupled Cu^{II} Complex with an EPR Spectrum of Mononuclear Cu^{II}: Effect of Alcoholic Solvents. *Inorg. Chem.* **2006**, *45* (22), 8841–8843. https://doi.org/10.1021/ic061186r.

(23) Sanakis, Y.; Pissas, M.; Krzystek, J.; Telser, J.; Raptis, R. G. Spin Relaxation in a Ferromagnetically Coupled Triangular Cu_3 Complex. *Chem. Phys. Lett.* **2010**, *493* (1–3), 185–190. https://doi.org/10.1016/j.cplett.2010.05.011.

(24) Boudalis, A. K.; Rogez, G.; Heinrich, B.; Raptis, R. G.; Turek, P. Towards Ionic Liquids with Tailored Magnetic Properties: $Bmim^+$ Salts of Ferro- and Antiferromagnetic Cu^{II}_3 Triangles. *Dalton Trans* **2017**, *46* (36), 12263–12273. https://doi.org/10.1039/C7DT02472J.

(25) Wang, L.-L.; Sun, Y.-M.; Yu, Z.-Y.; Qi, Z.-N.; Liu, C.-B. Theoretical Investigation on Triagonal Symmetry Copper Trimers: Magneto-Structural Correlation and Spin Frustration. *J. Phys. Chem. A* **2009**, *113* (39), 10534–10539. https://doi.org/10.1021/jp9045897.

(26) Sanakis, Y.; Pissas, M.; Krzystek, J.; Ozarowski, A.; Telser, J.; Raptis, R. G. Ferromagnetically-Coupled, Triangular, $[Bu_4N]_2[Cu^{II}_3(\mu_3\text{-}Br)_2(\mu\text{-}4\text{-}O_2N\text{-}Pz)_3Br_3]$ Complex Revisited: The Effect of Coordinated Halides on Spin Relaxation Properties. *Polyhedron* **2020**, *177*, 114258. https://doi.org/10.1016/j.poly.2019.114258.

(27) Yoon, J.; Solomon, E. I. Ground-State Electronic and Magnetic Properties of a μ_3-Oxo-Bridged Trinuclear Cu(II) Complex: Correlation to the Native Intermediate of the Multicopper Oxidases. *Inorg. Chem.* **2005**, *44* (22), 8076–8086. https://doi.org/10.1021/ic0507870.

(28) Ozarowski, A.; Calzado, C. J.; Sharma, R. P.; Kumar, S.; Jezierska, J.; Angeli, C.; Spizzo, F.; Ferretti, V. Metal–Metal Interactions in Trinuclear Copper(II) Complexes $[Cu_3(RCOO)_4(H_2TEA)_2]$ and Binuclear $[Cu_2(RCOO)_2(H_2TEA)_2]$. Syntheses and Combined Structural,

Magnetic, High-Field Electron Paramagnetic Resonance, and Theoretical Studies. *Inorg. Chem.* **2015**, *54* (24), 11916–11934. https://doi.org/10.1021/acs.inorgchem.5b02199.

(29) Belinsky, M. I. Spin-Frustrated Trinuclear Cu(II) Clusters with Mixing of 2(S = 1/2) and S = 3/2 States by Antisymmetric Exchange. 1. Dzialoshinsky−Moriya Exchange Contribution to Zero-Field Splitting of the S = 3/2 State. *Inorg. Chem.* **2008**, *47* (9), 3521–3531. https://doi.org/10.1021/ic701796q.

(30) Yvon, J.; Horowitz, J.; Abragam, A. Exchange Coupling Between Three Iron Ions in Two Organic Molecules. *Rev. Mod. Phys.* **1953**, *25* (1), 165–165. https://doi.org/10.1103/RevModPhys.25.165.

(31) Wucher, J.; Gijsman, H. M. Couplage de spins dans une molécule contenant trois ions chromiques. Propriétés magnétiques entre 1,6°K et 293°K de l'acétate complexe $[Cr_3(CH_3COO)_6(OH)_2]Cl.8H_2O$. *Physica* **1954**, *20* (1–6), 361–366. https://doi.org/10.1016/S0031-8914(54)80050-4.

(32) Long, G. J.; Robinson, W. T.; Tappmeyer, W. P.; Bridges, D. L. The Magnetic, Electronic, and Mössbauer Spectral Properties of Several Trinuclear Iron(III) Carboxylate Complexes. *J Chem Soc Dalton Trans* **1973**, No. 6, 573–579. https://doi.org/10.1039/DT9730000573.

(33) Murao, T. Jahn-Teller Effect in Trinuclear Complexes. *Phys. Lett. A* **1974**, *49* (1), 33–35. https://doi.org/10.1016/0375-9601(74)90657-4.

(34) Jones, D. H.; Sams, J. R.; Thompson, R. C. The Magnetic Behavior of Clusters of the Type $[M_3O(RCOO)_6]^+$. An Isotropic Model Involving Dynamic Distortions. *J. Chem. Phys.* **1984**, *81* (1), 440. https://doi.org/10.1063/1.447322.

(35) Rakitin, Yu. V.; Kalinnikov, V. T.; Novotortsev, V. M. Jahn-Teller Effect in Trigonal μ-Oxoclusters. *Russ. Chem. Bull.* **2004**, *53* (11), 2478–2484. https://doi.org/10.1007/s11172-005-0142-6.

(36) Rakitin, Yu. V.; Yablokov, Yu. V.; Zelentsov, V. V. EPR Spectra of Trigonal Clusters. *J. Magn. Reson. 1969* **1981**, *43* (2), 288–301. https://doi.org/10.1016/0022-2364(81)90039-1.

(37) Tsukerblat, B.; Belinskii, M.; Fainzil'berg, V. Magnetochemistry and Spectroscopy of Transition Metal Exchange Clusters. *Sov. Sci Rev B Harwood Acad Pub* **1987**, 337–482.

(38) Nishimura, H.; Date, M. Anomalous *g*-Value of a Cr-Trimer Complex, Cr-Propionate $\{Cr_3O(C_2H_5COO)_6(H_2O)_3\}NO_32H_2O$. *J. Phys. Soc. Jpn.* **1985**, *54* (1), 395–399. https://doi.org/10.1143/JPSJ.54.395.

(39) Honda, M.; Morita, M.; Date, M. Electron Spin Resonance in Cr-Trimer Complexes. *J. Phys. Soc. Jpn.* **1992**, *61* (10), 3773–3785. https://doi.org/10.1143/JPSJ.61.3773.

(40) Georgopoulou, A. N.; Margiolaki, I.; Psycharis, V.; Boudalis, A. K. Dynamic versus Static Character of the Magnetic Jahn–Teller Effect: Magnetostructural Studies of $[Fe_3O(O_2CPh)_6(Py)_3]ClO_4 \cdot py$. *Inorg. Chem.* **2017**, *56* (2), 762–772. https://doi.org/10.1021/acs.inorgchem.6b01912.

(41) Yoon, J.; Mirica, L. M.; Stack, T. D. P.; Solomon, E. I. Spectroscopic Demonstration of a Large Antisymmetric Exchange Contribution to the Spin-Frustrated Ground State of a D_3 Symmetric Hydroxy-Bridged Trinuclear Cu(II) Complex: Ground-to-Excited State Superexchange Pathways. *J. Am. Chem. Soc.* **2004**, *126* (39), 12586–12595. https://doi.org/10.1021/ja046380w.

(42) Ferrer, S.; Lloret, F.; Pardo, E.; Clemente-Juan, J. M.; Liu-González, M.; García-Granda, S. Antisymmetric Exchange in Triangular Tricopper(II) Complexes: Correlation among Structural, Magnetic, and Electron Paramagnetic Resonance Parameters. *Inorg. Chem.* **2012**, *51* (2), 985–1001. https://doi.org/10.1021/ic2020034.

(43) Erdös, P. Theory of Ion Pairs Coupled by Exchange Interaction. *J. Phys. Chem. Solids* **1966**, *27* (11–12), 1705–1720. https://doi.org/10.1016/0022-3697(66)90100-4.

(44) Yoon, J.; Solomon, E. I. Electronic Structures of Exchange Coupled Trigonal Trimeric Cu(II) Complexes: Spin Frustration, Antisymmetric Exchange, Pseudo-A Terms, and Their Relation to O2 Activation in the Multicopper Oxidases. *Coord. Chem. Rev.* **2007**, *251* (3–4), 379–400. https://doi.org/10.1016/j.ccr.2006.04.012.

(45) Bencini, A.; Gatteschi, D.; Bencini, A. *EPR of Exchange Coupled Systems*, Dover ed.; Dover Publications, Inc: Mineola, N.Y, 2012.

(46) Smith, T. D.; Pilbrow, J. R. The Determination of Structural Properties of Dimeric Transition Metal Ion Complexes from Epr Spectra. *Coord. Chem. Rev.* **1974**, *13* (2–3), 173–278. https://doi.org/10.1016/S0010-8545(00)80255-6.

(47) Coffman, R. E.; Buettner, G. R. General Magnetic Dipolar Interaction of Spin-Spin Coupled Molecular Dimers. Application to an EPR Spectrum of Xanthine Oxidase. *J. Phys. Chem.* **1979**, *83* (18), 2392–2400. https://doi.org/10.1021/j100481a018.

(48) Banci, L.; Bencini, A.; Gatteschi, D. Correlation between Anisotropic Exchange and Structure of Di-μ-Hydroxy Bridged Copper(II) Complexes. *J. Am. Chem. Soc.* **1983**, *105* (4), 761–764. https://doi.org/10.1021/ja00342a017.

(49) Bencini, A.; Gatteschi, D.; Zanchini, C. Anisotropic Exchange in Transition-Metal Dinuclear Complexes. 8. Bis(.Mu.-Pyridine N-Oxide)Bis[Dichloro(Dimethyl Sulfoxide)Copper(II)]. *Inorg. Chem.* **1986**, *25* (13), 2211–2214. https://doi.org/10.1021/ic00233a023.

(50) Boillot, M. L.; Journaux, Y.; Bencini, A.; Gatteschi, D.; Kahn, O. Single-Crystal EPR Study of $[Cu_2(Tert\text{-}Bupy)_4(N_3)_2](ClO_4)_2$ (Tert-Bupy = 4-Tert-Butylpyridine): Anisotropic Exchange in a Ferromagnetically Coupled Copper(II) Binuclear Complex. *Inorg. Chem.* **1985**, *24* (3), 263–267. https://doi.org/10.1021/ic00197a004.

(51) Bencini, A.; Gatteschi, D.; Reedijk, J.; Zanchini, C. Anisotropic Exchange in Transition-Metal Dinuclear Complexes. 4. (.Mu.-Benzotriazolato-N1,N3)Bis[[Tris(N1-Methylbenzimidazol-2-Ylmethyl)Amine-N,N3,N3',N3'']Copper(II)]Trinitrate. *Inorg. Chem.* **1985**, *24* (2), 207–209. https://doi.org/10.1021/ic00196a018.

(52) Magee, S. A.; Sproules, S.; Barra, A.-L.; Timco, G. A.; Chilton, N. F.; Collison, D.; Winpenny, R. E. P.; McInnes, E. J. L. Large Zero-Field Splittings of the Ground Spin State Arising from Antisymmetric Exchange Effects in Heterometallic Triangles. *Angew. Chem. Int. Ed.* **2014**, *53* (21), 5310–5313. https://doi.org/10.1002/anie.201400655.

(53) Piñero, D.; Baran, P.; Boca, R.; Herchel, R.; Klein, M.; Raptis, R. G.; Renz, F.; Sanakis, Y. A Pyrazolate-Supported Fe_3 (μ_3-O) Core: Structural, Spectroscopic, Electrochemical, and Magnetic Study. *Inorg. Chem.* **2007**, *46* (26), 10981–10989. https://doi.org/10.1021/ic0701460.

(54) Mathivathanan, L.; Boudalis, A. K.; Turek, P.; Pissas, M.; Sanakis, Y.; Raptis, R. G. Interactions between H-Bonded $[Cu^{II}_3(\mu_3\text{-}OH)]$ Triangles; a Combined Magnetic Susceptibility and EPR Study. *Phys. Chem. Chem. Phys.* **2018**, *20* (25), 17234–17244. https://doi.org/10.1039/C8CP02643B.

(55) Addison, A. W.; Rao, T. N.; Reedijk, J.; van Rijn, J.; Verschoor, G. C. Synthesis, Structure, and Spectroscopic Properties of Copper(II) Compounds Containing Nitrogen–Sulphur Donor Ligands; the Crystal and Molecular Structure of Aqua[1,7-Bis(N-Methylbenzimidazol-2′-Yl)-2,6-Dithiaheptane]Copper(II) Perchlorate. *J Chem Soc Dalton Trans* **1984**, No. 7, 1349–1356. https://doi.org/10.1039/DT9840001349.

(56) Hathaway, B. J.; Billing, D. E. The Electronic Properties and Stereochemistry of Mono-Nuclear Complexes of the Copper(II) Ion. *Coord. Chem. Rev.* **1970**, *5* (2), 143–207. https://doi.org/10.1016/S0010-8545(00)80135-6.

(57) Valko, M.; Mazúr, M.; Pelikán, P.; Kováčik, I.; Baran, P.; Valigura, D. Powder ESR Spectra of the Complexes [Cu(Phen)2X]ClO4 and [Cu(Bipy)2I]ClO4. *Collect. Czechoslov. Chem. Commun.* **1990**, *55* (7), 1660–1665. https://doi.org/10.1135/cccc19901660.

(58) Muthuramalingam, S.; Khamrang, T.; Velusamy, M.; Mayilmurugan, R. Catalytic Fixation of Atmospheric Carbon Dioxide by Copper(II) Complexes of Bidentate Ligands. *Dalton Trans.* **2017**, *46* (46), 16065–16076. https://doi.org/10.1039/C7DT03062B.

(59) Valko, M.; Morris, H.; Mazúr, M.; Telser, J.; McInnes, E. J. L.; Mabbs, F. E. High-Affinity Binding Site for Copper(II) in Human and Dog Serum Albumins (an EPR Study). *J. Phys. Chem. B* **1999**, *103* (26), 5591–5597. https://doi.org/10.1021/jp9846532.

(60) Halcrow, M. A. Interpreting and Controlling the Structures of Six-Coordinate Copper(II) Centres – When Is a Compression Really a Compression? *Dalton Trans* **2003**, No. 23, 4375–4384. https://doi.org/10.1039/B309242A.

(61) Esteves, C. V.; Lamosa, P.; Delgado, R.; Costa, J.; Désogère, P.; Rousselin, Y.; Goze, C.; Denat, F. Remarkable Inertness of Copper(II) Chelates of Cyclen-Based Macrobicycles with Two *Trans - N* -Acetate Arms. *Inorg. Chem.* **2013**, *52* (9), 5138–5153. https://doi.org/10.1021/ic400015v.

(62) Riplinger, C.; Kao, J. P. Y.; Rosen, G. M.; Kathirvelu, V.; Eaton, G. R.; Eaton, S. S.; Kutateladze, A.; Neese, F. Interaction of Radical Pairs Through-Bond and Through-Space: Scope and Limitations of the Point−Dipole Approximation in Electron Paramagnetic Resonance Spectroscopy. *J. Am. Chem. Soc.* **2009**, *131* (29), 10092–10106. https://doi.org/10.1021/ja901150j.

(63) Boča, R. *Theoretical Foundations of Molecular Magnetism*, 1st ed.; Current methods in inorganic chemistry; Elsevier: New York, 1999.

(64) Boudalis, A. K.; Rogez, G.; Turek, P. Determination of the Distributions of the Spin-Hamiltonian Parameters in Spin Triangles: A Combined Magnetic Susceptometry and Electron Paramagnetic Resonance Spectroscopic Study of the Highly Symmetric $[Cr_3O(PhCOO)_6(Py)_3](ClO_4)\cdot 0.5py$. *Inorg. Chem.* **2018**, *57* (21), 13259–13269. https://doi.org/10.1021/acs.inorgchem.8b01764.

(65) Clayton, J. A.; Keller, K.; Qi, M.; Wegner, J.; Koch, V.; Hintz, H.; Godt, A.; Han, S.; Jeschke, G.; Sherwin, M. S.; Yulikov, M. Quantitative Analysis of Zero-Field Splitting Parameter Distributions in Gd(III) Complexes. *Phys. Chem. Chem. Phys.* **2018**, *20* (15), 10470–10492. https://doi.org/10.1039/C7CP08507A.

(66) Brown, P.; Bushmelev, A.; Butts, C. P.; Cheng, J.; Eastoe, J.; Grillo, I.; Heenan, R. K.; Schmidt, A. M. Magnetic Control over Liquid Surface Properties with Responsive Surfactants. *Angew. Chem. Int. Ed.* **2012**, *51* (10), 2414–2416. https://doi.org/10.1002/anie.201108010.

(67) Gehlot, P. S.; Gupta, H.; Kumar, A. Paramagnetic Surface Active Ionic Liquids: Interaction with DNA and MRI Application. *Colloid Interface Sci. Commun.* **2018**, *26*, 14–23. https://doi.org/10.1016/j.colcom.2018.07.004.

(68) Klee, A.; Prevost, S.; Kunz, W.; Schweins, R.; Kiefer, K.; Gradzielski, M. Magnetic Microemulsions Based on Magnetic Ionic Liquids. *Phys. Chem. Chem. Phys.* **2012**, *14* (44), 15355. https://doi.org/10.1039/c2cp43048g.

(69) Georgopoulou, A. N.; Sanakis, Y.; Psycharis, V.; Raptopoulou, C., P.; Boudalis, A. K. Mössbauer Spectra of Two Extended Series of Basic Iron(III) Carboxylates $[Fe_3O(O_2CR)_6(H_2O)_6]A$ ($A^- = ClO_4^-, NO_3^-$). *Hyperfine Interact.* **2010**, *198*, 229–241. https://doi.org/10.1007/s10751-010-0179-2.

(70) Lin, C.-Y.; Ngendahimana, T.; Eaton, G. R.; Eaton, S. S.; Zadrozny, J. M. Counterion Influence on Dynamic Spin Properties in a V(IV) Complex. *Chem. Sci.* **2019**, *10* (2), 548–555. https://doi.org/10.1039/C8SC04122A.

Table of contents entry

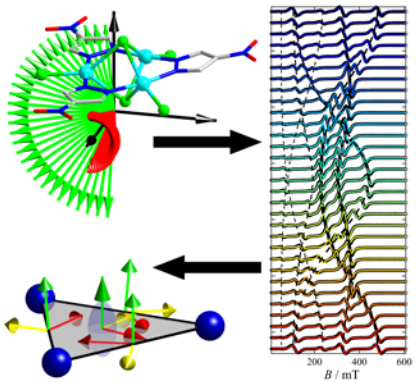

Single-crystal EPR experiments combined with *ab initio* calculations are used to rationalize the ferromagnetism of copper(II) triangles and to quantify the anisotropy induced by anisotropic exchange and dipolar interactions.